ABSTRACT

THE EFFECT OF PARTIAL SUBSTITUTION OF Ni BY Co AND Cu ON THE MAGNETIC AND MAGNETOCALORIC PROPERTIES OF THE INTERMETALLIC SYSTEM $Mn_{0.5}Fe_{0.5}Ni_{1-x}(CuCo)_xSi_{0.94}Al_{0.06}$

By Sharmistha Bhattacharjee

The magnetocaloric effect is a measure of the thermal change that magnetic materials experience when placed in an external magnetic field. Materials that exhibit large magnetocaloric effects can be used in magnetic refrigeration technology, which is significantly more energy efficient than the existing gas-based cooling technologies. Ongoing research in this field is focused on the development of magnetocaloric materials that are highly efficient, viable, and non-hazardous. In this thesis research, the structural, magnetic, and magnetocaloric properties of the Co and Cu doped intermetallic system, $Mn_{0.5}Fe_{0.5}Ni_{1-x}(CuCo)_xSi_{0.94}Al_{0.06}$ have been investigated. The materials were prepared by arc melting and annealing techniques, and their structural properties were studied by x-ray diffraction measurements. The diffraction patterns confirmed that all samples exhibited the single-phase hexagonal crystal structure. The phase purity and actual compositions of the alloys were confirmed by SEM micrographs. All the samples exhibited first-order phase transitions that were accompanied by thermal hysteresis. For a magnetic field change of 50 kOe peak entropy changes of up to -42.4 J kg^{-1} K^{-1} near 356 K were measured. For the corresponding material, a refrigeration capacity (RC) of 201 J/kg was calculated. The experimental data and detailed discussion of the experimental results are presented in this thesis.

THE EFFECT OF PARTIAL SUBSTITUTION OF Ni BY Co AND Cu ON THE MAGNETIC AND MAGNETOCALORIC PROPERTIES OF THE INTERMETALLIC SYSTEM $(Mn_{0.5}Fe_{0.5})Ni_{1-x}(CuCo)_xSi_{0.94}Al_{0.06}$

A Thesis

Submitted to the

Faculty of Miami University

in partial fulfillment of

the requirements for the degree of

Master of Science

by

Sharmistha Bhattacharjee

Miami University

Oxford, Ohio

2023

Advisor: Dr. Mahmud Khan

Reader: Dr. Samir Bali

Reader: Dr. Perry Corbett

This thesis titled

THE EFFECT OF PARTIAL SUBSTITUTION OF Ni BY Co AND Cu ON THE MAGNETIC AND MAGNETOCALORIC PROPERTIES OF THE INTERMETALLIC SYSTEM $(Mn_{0.5}Fe_{0.5})Ni_{1-x}(CuCo)_xSi_{0.94}Al_{0.06}$

by

Sharmistha Bhattacharjee

has been approved for publication by

The College of Arts and Science

and

The Department of Physics

Dr. Mahmud Khan

Dr. Samir Bali

Dr. Perry Corbett

Table of Contents

List of Figures

List of Tables

Dedication

This thesis is dedicated to my beloved mother.

Acknowledgment

I would like to express my deepest gratitude to my advisor Dr. Mahmud Khan for his continuous support and guidance in completing the thesis and throughout my stay at Miami University. Thank you to Dr. Arjun Pathak and his group at Buffalo State University SUNY for their support to measure various experimental data reported in this work. I would also like to thank Dr. Samir Bali and Dr. Perry Corbett for being my thesis committee members. I also appreciate the friendly atmosphere in the lab with my lab mates Kyra Stillwell and Brandon Reese.

Chapter 1: Introduction

Magnetic refrigeration (MR) is an emerging eco-friendly technology that directly addresses the current global concern of improving energy efficiency.[1,2] The technology relies on special types of solid-state magnetic refrigerants that exhibit large magnetocaloric effects (MCE), which is signified by the thermal change of a material when an external magnetic field is applied. Since Percharsky and Gschneidner reported a giant MCE near room temperature in $Gd_5(Si_2Ge_2)$ in the late 90s,[3] numerous other materials that exhibit large MCEs have been discovered and tested for their application potential.[4,5,6,7,8] Although thousands of materials with a considerable amount of MCEs have been reported, only a handful of these materials are considered suitable for application in a practical magnetic refrigeration system.[8,9] The remaining compounds are either toxic or contain rare and expensive constituents. Materials that exhibit first-order magnetic phase transitions (FOMPT) exhibit additional drawbacks including thermal and magnetic hysteresis. This is a significant source of efficiency losses that hinders the reversibility of the adiabatic temperature change, which is required for the efficient operation of the cooling cycle.[10,11] Discovery of new materials that are free of these drawbacks and are constituted of cheap, readily available materials is crucial for making the commercialization of MR possible.

The magnetocaloric effect is associated with ordering of magnetic moments in a magnetic material. The total entropy of a magnetic material can be expressed as the sum of the lattice entropy, magnetic entropy, and electronic entropy and can be written as: [12,13],

$$S(T,H) = S_M(T,H) + S_L(T) + S_{EL}(T)$$

When a magnetic material is placed in an external magnetic field, the magnetic moments align with the field resulting in a decrease in the magnetic entropy of the system. If this process is done at a finite temperature (adiabatically), the decrease of the magnetic entropy would cause an increase in the lattice entropy of the system to keep the total entropy constant. The increase of the lattice entropy increases the lattice vibration causing an increase in the temperature of the material. If heat is removed from the material followed by the removal of the magnetic field, the magnetic entropy would increase and go back to the initial state. This would cause the lattice entropy to decrease, and since heat was already removed from the system, the

material would absorb heat from the surroundings to bring the lattice entropy back to its initial state. A sketch of this process is shown in Fig.1.1.

Materials that exhibit large magnetic entropy changes 'ΔS_M' near room temperature is desired for the MR technology[14]. For a given magnetic material ΔS_M is maximum near the magnetic phase transition. For a ferromagnetic material, this transition is the ferromagnetic to paramagnetic phase transition that occurs at Curie temperature, Tc. Generally, the ferromagnetic transition is a second-order phase transition, but for some materials, the ferromagnetic transition is accompanied by a structural phase transition. In this case, the transition is a first-order phase transition, where the entropy changes under heating and cooling do not coincide due to the existence of thermal hysteresis.[15] This is unlike the ΔS_M observed in materials with second-order phase transitions that are not accompanied by any thermal hysteresis. The materials that are being studied in this thesis exhibit first-order phase transitions.

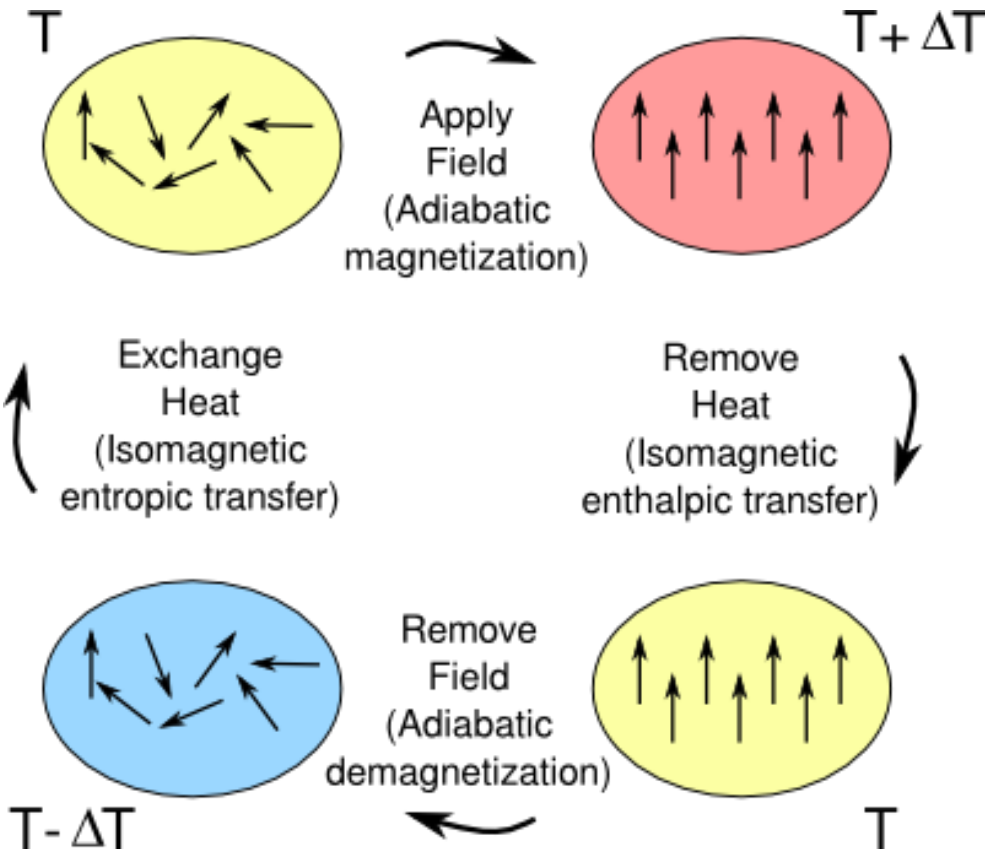

Fig. 1.1. The thermodynamic cycle of a magnetic refrigerator.[16]

This thesis research is motivated by the magnetocaloric effect of recently reported (Mn,Fe)-Ni-(Si,Al) based intermetallic systems. The materials exhibit ΔS_Ms of as large as $-63.2\ \mathrm{J\,kg^{-1}\,K^{-1}}$ (for a field change of 50 kOe) near room temperature.[17,18,19] The large MCEs in these compounds are associated with the FOMPT that occurs between a Ni_2In type hexagonal phase and a TiNiSi-type orthorhombic phase.[20] As typical for FOMPTs, the ΔS_M's in the (Mn,Fe)-Ni-(Si,Al) materials are accompanied by large thermal and magnetic hysteresis.[18] Biswas et al. reported the ΔS_M for the $Mn_{0.5}Fe_{0.5}NiSi_{1-x}Al_x$ ($0.05 \leq x \leq 0.07$) system where the transition temperatures (T_C) ranged between 200 K and 320 K. For x =0.07, peak ΔS_M of $-23\ \mathrm{J\,kg^{-1}K^{-1}}$ was observed at T = 205 K for a field change of 20 kOe. Melt-spun ribbons of $Mn_{0.5}Fe_{0.5}NiSi_{1-x}Al_x$ have been reported to enhance the T_C but reduce the peak ΔS_M.[21] The covalent bonding between the T and X atoms and the interatomic distances between the Mn atoms are believed to be the primary control parameters for the stability of the crystalline structure (hexagonal or orthorhombic) of the MnTX compounds.[20] Since the thermal and magnetic hysteresis is strongly dependent on the stability of the crystal structure near the phase transition, it is interesting to investigate new (Mn,Fe)-Ni-(Si,Al) materials with altered stoichiometry.[20,22,23,24,25]

In this thesis, the effect of partially replacing Ni with Co and Cu on the structural, magnetic, and magnetocaloric properties of $(Mn_{0.5}Fe_{0.5})Ni_{1-x}Co_xSi_{0.94}Al_{0.06}$ and $(Mn_{0.5}Fe_{0.5})Ni_{1-x}Cu_xSi_{0.94}Al_{0.06}$ have been investigated. These systems are the Co and Cu derivative of the $Mn_{0.5}Fe_{0.5}NiSi_{0.94}Al_{0.06}$ compound that showed a T_C of ~265 K and a peak ΔS_M of $\sim -20\ \mathrm{J\,kg^{-1}K^{-1}}$.[19] The goal of the project is to develop materials that show optimized MCE that is useful for MR technology. The research involved sample preparation and characterization and the thesis is divided in the following manner. Chapter 2 provides a brief background and literature review related to the research. Details on the experimental methods are discussed in Chapter 3. The results and discussion are presented in Chapter 4, and Chapter 5 concludes the thesis.

Chapter 2: A Brief Background

2.1 Basic Concepts of Magnetism

Magnetism arises from two different sources. The motion of the electrons in an orbit around the nucleus, and the other is the spin of the electrons around its axis, analogous to the rotation of the Earth about its own axis.[26] The strength of the magnetic field is measured by the magnetic moment of a magnet which is defined by the rotational force experienced by it in a magnetic field of unit strength acting perpendicular to its magnetic axis. It can be expressed mathematically by the equation given below:

$$\boldsymbol{t} = \mu \times \boldsymbol{B}$$

$\boldsymbol{t}$ represents the torque of alignment caused by $\boldsymbol{B}$ (applied magnetic field), and μ represents the magnetic moment of an atom.

In an atom with completely filled electronic shells, the magnetic moment of the electrons cancels out due to the zero net spins. This is due to the Pauli Exclusion Principle that states, "each electronic orbit can be occupied by only two electrons of opposite spin". Only the atoms with unfilled electron shells exhibit a net magnetic moment.

The magnetic properties of a material depend on the crystal structure and electronic configuration of the constituent atoms. Based on magnetic ordering, (See Fig. 2.1) materials can be classified into five major categories: diamagnetism, paramagnetism, ferromagnetism, antiferromagnetism, and ferrimagnetism.[27] The magnetic susceptibility denoted by χ, - is a measure of the degree of the magnetization of the material when placed in an external magnetic field.

$$X = \frac{\mu_o M}{B} = \frac{M}{H}$$

Here μ_o is the electromagnetic permeability of free space, M denotes the magnetization which is the response to the magnetic field of strength B, and H is the intensity of the applied magnetic field.[28]

Materials that are made up of atoms with completely filled electron shells exhibit diamagnetic behavior. Diamagnetic materials are often considered non-magnetic as they have no net magnetic moment without the presence of an external magnetic field. Induced magnetization is generated in the opposite direction of the applied magnetic field.[29,30] Therefore, negative magnetization is produced in diamagnetic materials and magnetic susceptibility (χ) for these materials is below zero.

Paramagnetism occurs in materials with atoms unfilled electron shells. When an external field is applied to these materials, some atomic magnetic moments rotate and align along the field direction, resulting in a small net magnetization and positive susceptibility.[31] The magnetic dipole moments of ferromagnetic materials tend to align in the same direction. As a result, magnetic susceptibility increases to a great extent. Ferromagnetic materials have permanent magnetization. Due to the strong interactions in the magnetic moments, they show very large net magnetization under the application of a much smaller magnetic field. These interactions are produced by electronic exchange forces and result in a parallel or antiparallel alignment of atomic moments.[32] The magnetization of ferromagnetic material is temperature dependent. As the temperature increases the spin order is destroyed by thermal agitation.[33] As a result, at high-temperature magnetization of the ferromagnetic material starts reducing and eventually becomes zero. Magnetic susceptibility is inversely proportional to the temperature, which is described by the Curie-Weiss law. [32,33] The temperature at which magnetization becomes zero and ferromagnetic materials behave like a paramagnetic is called Currie temperature T_c.

Antiferromagnetic materials have permanent magnetic moments but with a strong, negative interaction between them due to the antiparallel orientation of the neighboring magnetic moments as a result, there is no net or spontaneous magnetization when they are all perfectly aligned. Below a critical temperature, T_N (Neel temperature), antiferromagnetic materials spontaneously align themselves into antiparallel arrangements throughout the material so that they exhibit no net magnetic moments.[34] In these materials, the spontaneous antiparallel coupling of atomic magnets is disrupted by heating and disappears entirely above the Neel temperature. [35] Ferrimagnetic behavior is normally observed typically in transition metal oxides. Like ferromagnets, they exhibit a spontaneous magnetization below the critical temperature, Tc, even in the absence of an applied field. However, the net ferrimagnetic moment arises from the incomplete cancellation of spin moments. Because, unlike antiferromagnets, the two sublattices are not identical. The magnetic moments of one sublattice

are greater than that of the oppositely oriented sublattice. As a result, ferrimagnetic materials exhibit net magnetization in zero magnetic fields.[36,37] More detailed information can be found in the reference.[31]

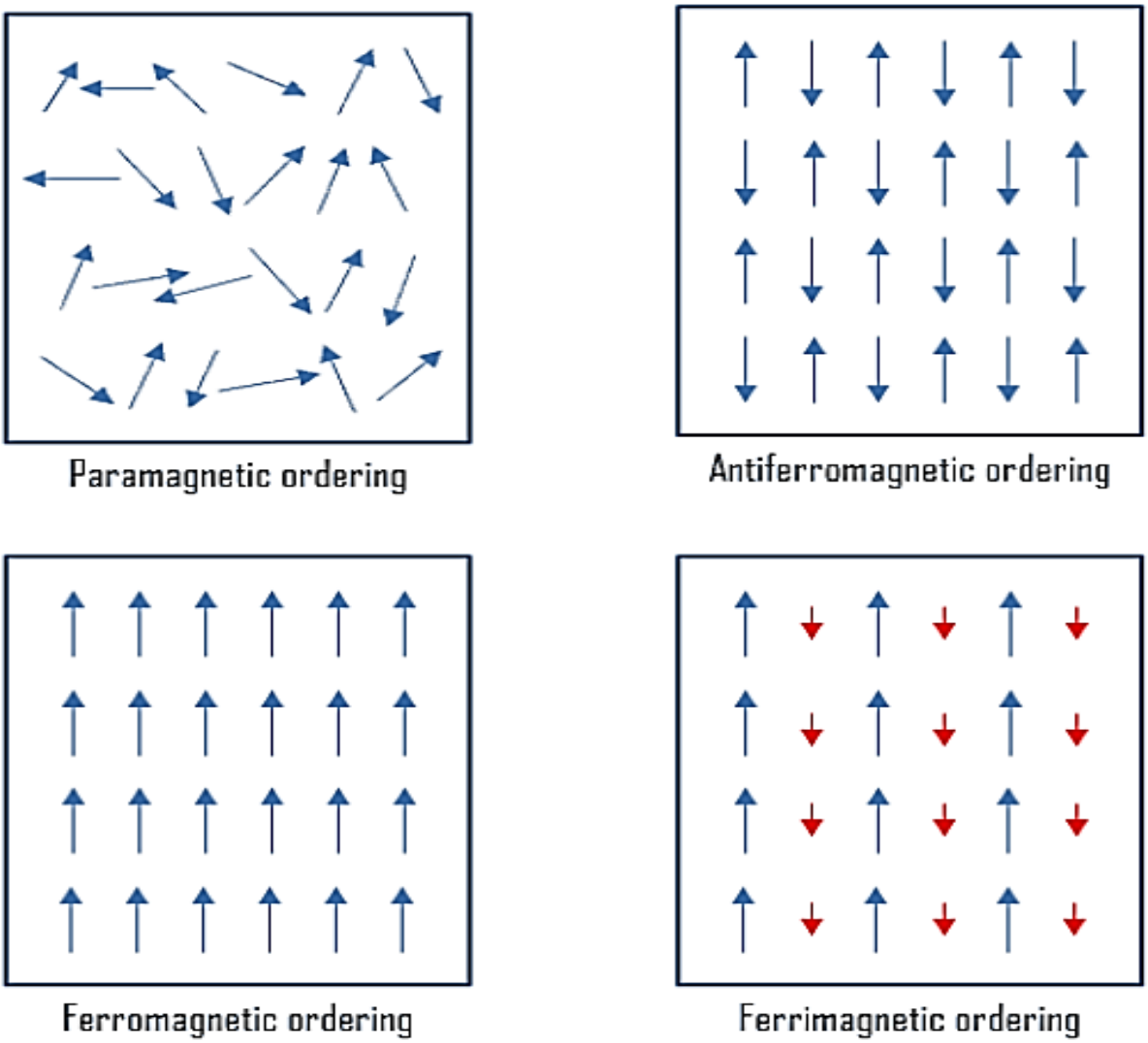

Fig. 2.1. Different magnetic ordering inside materials.[35]

Hysteresis Loop

The magnetic response of a ferromagnetic material in an applied magnetic field can generally be demonstrated by a hysteresis loop as shown in Fig. 2.2. Starting with a nonmagnetic state (domains randomly aligned), magnetization increases as the field is increased. The magnetization reaches the maximum value (saturation magnetization, M_S) when all the spins are aligned with the field. After that, if the applied field is reduced the magnetization does not follow the initial curve, because the exchange interaction of the magnetic domain prevents the domains to return to the initial orientation.[34] The residual magnetization, M_r, is the magnetization remaining in the material after the field returns to zero. A sufficiently large

magnetic field in the reverse direction must be applied before the magnetization process can be reversed.

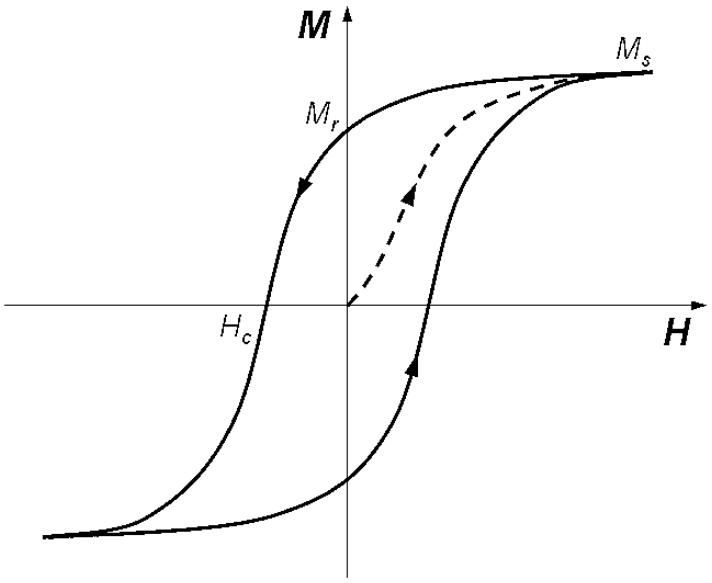

Fig. 2.2. A typical magnetic hysteresis loop of ferromagnetic material.[38]

where M_S is the saturation magnetization, maximum magnetization which does not increase with increasing magnetic field H. Residual magnetization M_R, magnetization remaining at zero fields. Coercivity H_C, the magnetic field needed to be applied to remove the induced magnetization.

2.2 Magnetic Exchange Interaction

The magnetic moments of neighboring atoms go through parallel or antiparallel arrangements due to the presence of exchange interaction forces among them. When the arrangement is parallel, it shows the ferromagnetic behavior and anti-parallel alignment represents the antiferromagnetic behavior. These interactions occur between two neighboring particles through a quantum mechanical process. The wave functions of the indistinguishable particles exhibit exchange symmetry. This implies that when the two particles are exchanged, their wave function remains unchanged. Exchange interaction is in fact a consequence of the Pauli exclusion principle.[39] If we consider two electrons which are fermions, these electrons are forbidden from assuming the same quantum state because the Pauli Exclusion principle states that no two or more identical electrons can occupy the same quantum state. Magnetic exchange interactions include direct exchange interaction, Indirect exchange interaction, super exchange interaction, and double exchange interaction.

2.2.1 Direct Exchange Interaction

Direct exchange interaction (Fig. 2.3) involves an overlap of electrons wavefunction between the neighboring atoms and Coulomb electrostatic repulsion. Direct exchange is strong, but short-range interaction. If the distance between the atoms increases, the interaction between their electrons decreases. The Heisenberg Hamiltonian for the exchange interaction in the many-electron atomic system can be expressed as: [40]

$$H_{ex} = -2J_{ex}S_i.S_j$$

where S_i and S_j are dimensionless spin operators and J_{ex} is the exchange energy. According to Bethe and Slater, if the distance between two atoms is small, the two electrons stay within their interatomic gap to minimize the Coulomb repulsion. The electrons are then forced to assume opposite spins. This results in negative exchange energy due to antiparallel spin ($J_{ex} < 0$ gives antiferromagnetism) because of the Pauli exclusion principle: no two electrons can have the same set of quantum numbers. When the orbital wave function is symmetrical the spins must be antisymmetric and vice versa. When the interatomic distance is larger, to minimize the coulomb repulsion, the electrons stay far away from each other, and that results in a positive exchange due to the parallel arrangement ($J_{ex} > 0$ gives ferromagnetism).

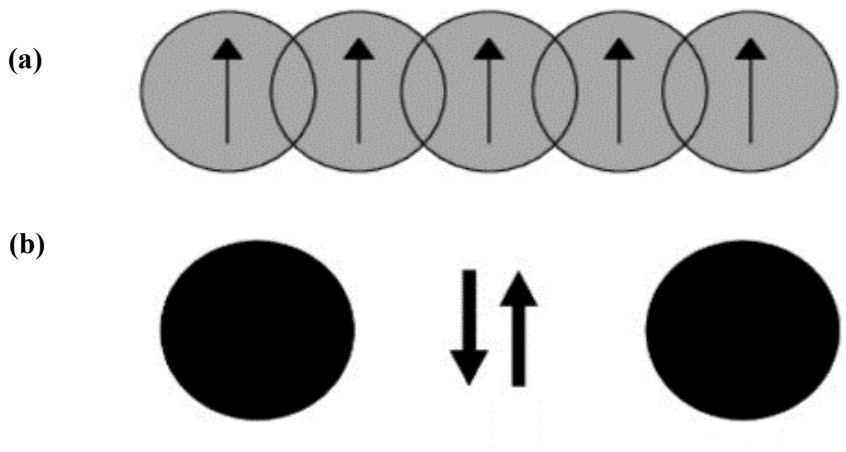

Fig. 2.3(a). Parallel arrangement for large interatomic distances (b) Antiparallel arrangement for small interatomic distances.[12]

2.2.2 Indirect Exchange Interaction

Indirect interaction occurs when the interatomic distance between the neighboring atoms is large so that wavefunctions of electrons cannot overlap directly. In 1954, Kittel and Ruderman

first proposed the theory of indirect exchange interaction and later Kasuya and Yoshida further advanced the Theory. This interaction is also called RKKY named after Ruderman, Kittel, Kasuya, and Yoshida which involves a coupling of magnetic moments or localized inner d- or f-shell electron spins in a metal by means of interaction through the conduction electrons. A spin polarization in the conduction electrons is induced by the magnetic ion on its surroundings and other magnetic ions feel this spin polarization in the itinerant electrons that ultimately leads to an indirect coupling. The strength of the RKKY coefficient depends on the interatomic spacing. This implies that magnetic moments in a metallic compound can either be ferromagnetically or antiferromagnetically coupled depending on the distance between them.[13]

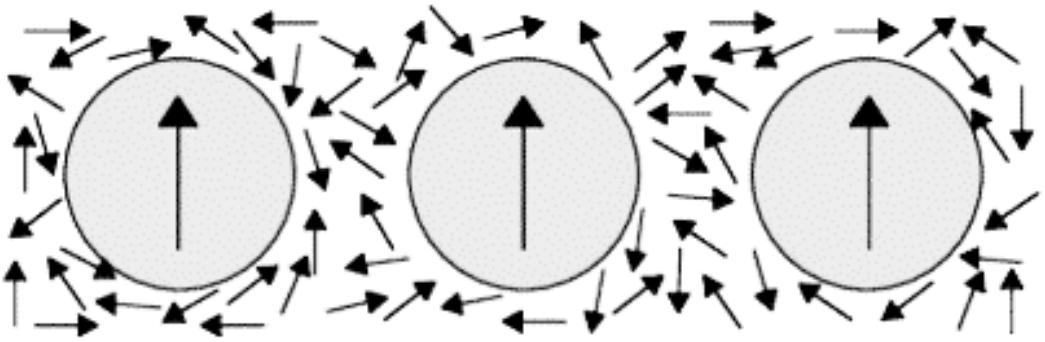

Fig. 2.4. Indirect exchange interaction via conduction electrons

2.2.3 Superexchange Interaction

Superexchange interaction occurs between moments on ions too far apart to be connected by the direct exchange but coupled over a relatively long distance through a non-magnetic material. It is basically the strong coupling between two cations with a nonmagnetic anion.[41] The coupling can be either ferromagnetic or antiferromagnetic depending upon the type of interaction. The superexchange phenomenon was first proposed by Hendrik Kramers in 1934. It was further developed by Phillip Anderson in 1950. The idea can be illustrated by the structure $Mn^{2+} - O^{2-} - Mn^{2+}$. Along each chain direction, the O^{2-} ion has an occupied p orbital oriented *along the Mn–O–Mn axis, as shown in Figure:*

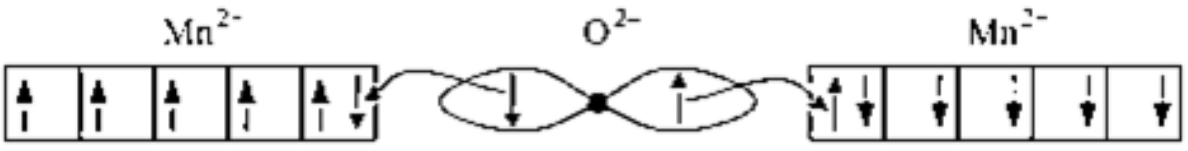

Fig. 2.5. Example of Superexchange Interaction in MnO crystal.[29]

Each Mn^{2+} ion contains five 3d electrons, which occupy the 3d orbitals with one electron per orbital. Since the O^{2-} ion has a filled shell of electrons, hybridization can only take place by the donation of electrons from the O^{2-} ion into the vacant orbitals of the Mn^{2+} ion. Let's assume that our left-most Mn^{2+} ion has an up-spin, as shown in Figure.[29]

Then, since all the Mn orbitals contain an up-spin electron already, covalent bonding can only occur if the neighboring oxygen donates its down-spin electron. This leaves an up-spin electron in the oxygen p orbital, which it can donate to the next Mn^{2+} ion in the chain. By the same argument, bonding can only occur if the electrons on the next Mn^{2+} ion are down-spin. This oxygen-mediated interaction leads to an overall antiferromagnetic alignment. [42,43]

2.2.4 Double Exchange Interaction

The double exchange mechanism was first proposed in 1951 by Clarence Zener to account for electrical transport properties.[44] Double exchange interaction occurs when electrons from one magnetic atom are exchanged with another magnetic atom with a non-magnetic atom acting as an intermediary in this transfer. The double exchange is different from the superexchange interaction because the magnetic ions are in different oxidation states with one ion having more electrons than the other, but in superexchange with magnetic ions have the same valance electron configuration. Double exchange interaction can be illustrated by the MnO system. The Mn atoms are in different oxidation states, (Mn^{4+} and Mn^{3+} ions). If O gives up its spin-up electron to Mn^{4+}, its vacant orbital can then be filled by an electron from Mn^{3+}. The electrons transferred between neighboring Mn ions must possess the same spin according to Pauli's principle. In order to conform with Hund's rules interaction, the unpaired electrons of the Mn cations change their spin direction parallel to the transmitted electron. The double exchange interaction is energetically favorable when the transferred electron doesn't need to reorient itself. Overall, it leads to the ferromagnetic alignment of neighboring ions.

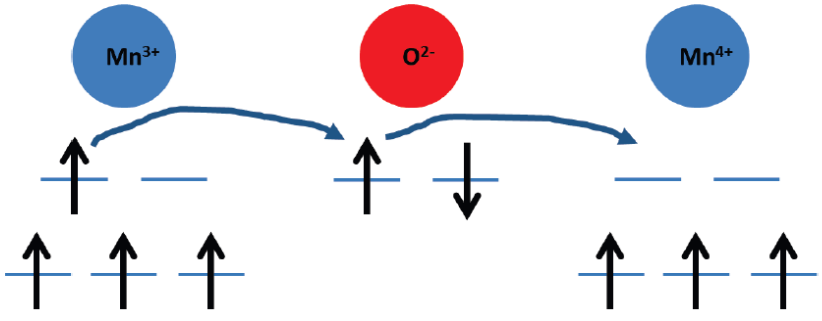

Fig. 2.6. Example of Double Exchange Mechanism in MnO[13]

2.3 The Magnetocaloric Effect

The magnetocaloric effect refers to the change of the thermodynamic state of a magnetic material by the application of an external magnetic field. It was discovered by the German physicist E. Warburg in 1881. He observed heat generated under the application of a magnetic field in iron.[45] In 1918 Weiss and Piccard[46] experimentally discovered MCE in nickel where they reported a reversible temperature change in Nickel close to its Curie temperature using a 1.5 T external magnetic field. This idea was further advanced by Debye and Giauque.[47] The first application of the phenomenon was demonstrated by Giauque and McDougal to apply the MCE to achieve sub-Kelvin temperatures (0.25 K).[48] By applying a 0.8 T magnetic field and cooling a paramagnetic $Gd_2(SO_4)_3.8H_2O$ salt by liquid He to 1.5 K they magnetized the salt. When the field was removed, the salt containing Gd became demagnetized and cooled down. Later in 1976, G.V Brown demonstrated the feasibility of room-temperature magnetic refrigeration by developing the first prototypes of a practical magnetic refrigerator that can operate at room temperature. Using the Gd metal, Brown achieved a temperature span of 47 K after 50 cycles without a heat load. Pure Gd is a rare earth element that is very expensive and non-abundant which reduces its commercial application for MCE. Following the discovery of the giant magnetocaloric effect in $Gd_5(Si_2Ge_2)$ in 1997 by Pecharsky and Gschneider[49], the focus has shifted to identifying new materials for potential use as refrigerants in devices operating near room temperature.

2.3.1 Thermodynamic Model of Magnetocaloric Materials

MCE can be explained by using a thermodynamics system and applying the first law of thermodynamics. The total internal energy of the system can be described as a function of the external magnetic field *(H),* the volume *(V),* and the entropy *(S)* of the system.[50]

$$U = U\,(S, V, H)$$

and can also be written as a function of the magnetic moment (M), V, and S

$$U=U\,(S,\ V,\ M)$$

The corresponding differential equation of U has the forms:

$$dU=TdS - pdV - MdH \quad (1.1)$$

$$dU= TdS - pdV - HdM \quad (1.2)$$

Here, H is the applied field, M is the magnetization, p and T denote the pressure, and temperature respectively.

According to the first law of thermodynamics for a closed system, if heat is added or if work is done then the internal energy of the magnetocaloric material will increase.[51] This law can be written as follows:

$$dU = dq + dW \quad \text{(1.3)}$$

Where W is the amount of work done on the system and q is the quantity of heat that is added to the system. In a reversible process, the second law of thermodynamics can be written as:

$$dq = TdS \quad \text{(1.4)}$$

When the external magnetic field is applied, due to the alignment of the magnetic dipole moment the material becomes magnetized, and it will start to produce its own magnetic field. The work required to magnetize the magnetocaloric material can be expressed as:

$$dW = \mu_o H\, dM \quad \text{(1.5)}$$

Considering the volume of the magnetic field is fixed, equation 1.3 can be written as:

$$dU = T\, dS + \mu_o H\, dM \quad \text{(1.6)}$$

Where $\mu_\circ$ is the permeability in a vacuum. For isobaric and isochoric processes, the derivative of the total entropy of the system can be expressed as a function of temperature and applied magnetic field strength as:

$$dS\,(T,H) = \left(\frac{\delta S}{\delta T}\right)_H dT + \left(\frac{\delta S}{\delta H}\right)_T dH \quad \text{(1.7)}$$

Using equations 1.4, 1.6, and 1.7, the specific heat of the system can be derived as:

$$C_T = \left(\frac{\delta q}{\delta H}\right)_T = T\left(\frac{\delta S}{\delta H}\right)_T \quad \text{(1.8)}$$

$$C_H = \left(\frac{\delta q}{\delta T}\right)_H = T\left(\frac{\delta S}{\delta T}\right)_H \quad \text{(1.9)}$$

From Equation 1.4 it can be written as:

$$dq = C_T(T,H)dH + C_H(T,H)dT \quad \text{(2.1)}$$

Using the Maxwell relation equation (1.8) can be rewritten as:

$$C_T = T\left(\frac{\delta S}{\delta H}\right)_T = \mu_o T\left(\frac{\delta M}{\delta T}\right)_H \quad \text{(2.2)}$$

Isothermal Magnetic Entropy Change

In an isothermal process, the temperature of the system remains constant *(dT=0)*. Then the total entropy changes of the system in equation 1.7 can be rewritten as:

$$dS = \left(\frac{\delta S}{\delta H}\right)_T dH \quad \text{(2.3)}$$

Now from equation 2.2, it can be written as:

$$\left(\frac{\delta S}{\delta H}\right)_T = \mu_o \left(\frac{\delta M}{\delta T}\right)_H \quad \text{(2.4)}$$

The entropy change in the isothermal process can be rewritten as:

$$dS(T,H) = \left(\frac{\delta S}{\delta H}\right)_T dH$$

$$dS(T,H) = \mu_o \left(\frac{\delta M}{\delta T}\right)_H dH \quad \text{..... (2.5)}$$

When the applied magnetic field varies from H_1 *to* H_2 considering isothermal conditions, the isothermal entropy change can be defined as follows:

$$\Delta S_M = S_2 - S_1$$

$$\Delta S_M = \int_{H_1}^{H_2} \left(\frac{\delta S}{\delta H}\right)_T dH$$

$$\Delta S_M = \int_{H_1}^{H_2} \mu_o \left(\frac{\delta M}{\delta T}\right)_H dH \quad \text{.....(2.6)}$$

$$\Delta S_M = \int_{H_1}^{H_2} \frac{C_T}{T} dH \quad \text{..... (2.7)}$$

where H_1 and H_2 are the initial and final applied magnetic fields and S_1 and S_2 represent the corresponding entropy changes. The sign of ΔS_M is determined by the sign of the derivatives. If ΔS_M is negative, it is denoted as direct MCE. While if it is positive, it is known as inverse MCE. In the case of negative ΔS_M, the material heats up when magnetized and cools down when demagnetized. Conversely, a material with positive ΔS_M cools down when magnetized.[40]

Adiabatic Temperature Change

To characterize the magnetocaloric material another important parameter will be used. This is called adiabatic temperature change T_{ad}. In an adiabatic process, there is no heat flow between the system and the environment. The total entropy change of the system remains constant under adiabatic conditions. Therefore, any change in the applied field leads to a proportional change in the temperature of the material. From equation 1.7:

$$\left(\frac{\delta S}{\delta T}\right)_H dT + \left(\frac{\delta S}{\delta H}\right)_T dH = 0 \quad \text{..... (2.8)}$$

Or it can be expressed as:

$$\left(\frac{\delta S}{\delta T}\right)_H dT = -\left(\frac{\delta S}{\delta H}\right)_T dH = \mu_o \left(\frac{\delta M}{\delta T}\right)_H dH \quad \text{..... (2.9)}$$

From equation

$$\frac{C_H}{T} = \left(\frac{\delta S}{\delta T}\right)_H = -\mu_o \left(\frac{\delta M}{\delta T}\right)_H \quad \text{..... (2.10)}$$

The equation for adiabatic temperature change can be written as

$$\Delta T_{adiabetic} = \int_{H_1}^{H_2} \frac{-T\mu_o}{C_H} \left(\frac{\partial M}{\partial T}\right)_H dH \quad \text{..... (3.1)}$$

$$\Delta T_{adiabetic} = -T\frac{\mu_o}{C_H}\int_{H_1}^{H_2}\left(\frac{\partial M}{\partial T}\right)_H dH \ldots\ldots\ldots\ldots\ldots\ldots\ldots\ldots\ldots\ldots \quad (3.2)$$

The negative sign of the equation ensures the fact that the magnetization of the material decreases with the increase of temperature in the material, regardless of the applied field strength. Any material should have the largest magnetic entropy and adiabatic temperature change when its magnetization changes rapidly with temperature, i.e in the vicinity of a phase transition temperature. The maximum MCE can measure near phase transition temperature and gradually decreases both below and above the phase transition temperature The magnetocaloric effect can be measured directly from adiabatic temperature change or calculated indirectly from the measured magnetization or heat capacity, both as a function of temperature and magnetic field. Isothermal magnetic entropy changes and adiabatic temperature changes, both characteristics of the magnetocaloric effect are dependent on material.

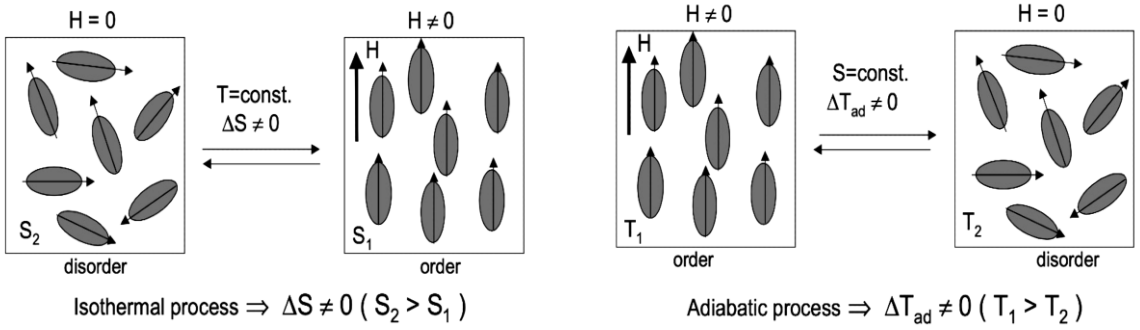

Fig. 2.7. Adiabatic temperature and isothermal entropy.[12]

2.4 Magnetic Phase Transition

A phase transition is said to occur when magnetic material goes from one phase or state of magnetic ordering to another. The magnetization M, which defines the MCE, also depends on the phase transformations. For ferromagnetic materials a temperature induced phase transformation from a ferromagnetic state to a paramagnetic state occurs at the Curie temperature, T_c. Phase transition in magnetic materials is generally classified as either a first-order phase transition (FOMPT) or a second order phase transition (SOMPT). Paul Ehrenfest provided a conceptually simple definition of the order of a phase transition by the behavior of their Helmholtz free energy (F) as:

$$dF = -SdT - MdH$$

For a constant temperature, the equation can be written as:

$$M = -\left(\frac{\delta F}{\delta T}\right)_T$$

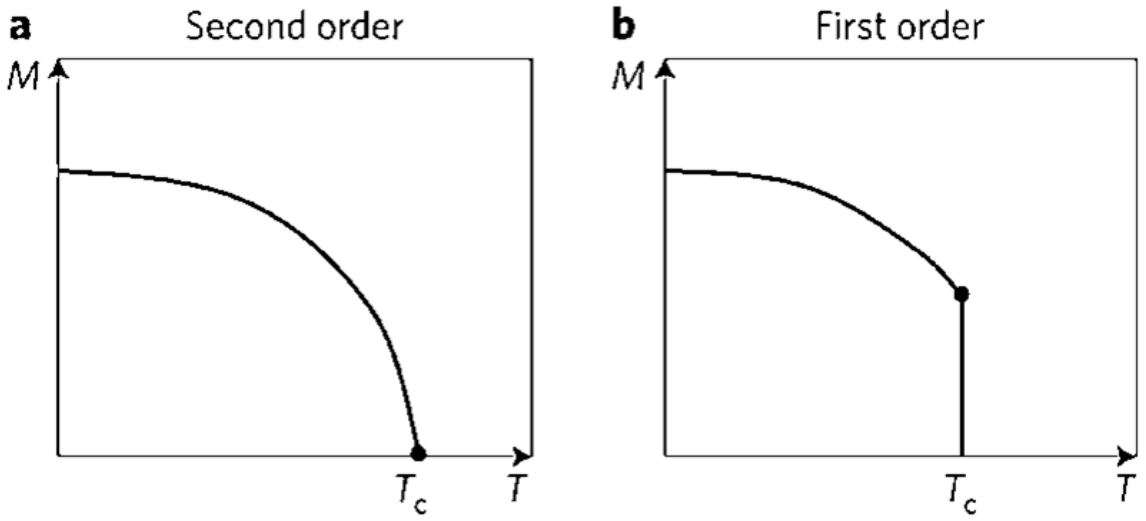

Fig. 2.8. Schematic diagram of Phase transition. (a) First-order phase transition (b) Second-order phase transition.

A first-order phase transition is associated with a discontinuity with the first derivative of Helmholtz free energy with respect to some thermodynamic variable.[50] These include volume, magnetization, and entropy of the material. FOMPT involves latent heat. In many cases, the first-order transition is associated with the crystalline structure and magnetic phase transition (Ferromagnetic to Paramagnetic). FOMPT materials have the advantages of exhibiting large magnetic entropy changes and adiabatic temperature change, which are desired for MCE, but these materials are accompanied by thermal and magnetic hysteresis. During the phase transition, discontinuous changes in volume and thermal stress make the FOMPT materials susceptible to cracking. Due to latent heat, hysteresis leads to lower efficiency and reduces the reversibility of the FOMPT materials.[52] Although the FOMPT materials are theoretically the most appropriate for MCE applications, these limitations hinder the application of the FOMPT materials.

Second-order phase transition (SOMPT) is associated with discontinuities in the second derivative of the Helmholtz free energy. No latent heat is involved in SOMPT. The magnetization changes continuously in SOMPT materials and goes to zero above the Currie temperature T_c. The advantage of SOMPT materials is they do not suffer from thermal hysteresis but their magnetocaloric responses are usually smaller than most of the FOMPT materials when operating within the same temperature range.[53] However, the high cost,

susceptibility to corrosion, and uneven transition temperatures of SOMPT materials have reduced their implementation in MCE applications.

Previous discussions have indicated the most important thermodynamic variable required to understand the mechanism of FOMPT and SOMPT. The distinction between first and second-order phase transition is that in first-order phase transition, the thermodynamic system's entropy, volume, and energy change abruptly, but in second-order phase transition, the system's entropy, volume, and energy change gradually.[54] It is not possible for crystal to change instantaneously, the transition must start from the formation of a microscopic nucleus in the crystal. Nucleation, a well-known quantity in thermodynamic phase transition study, is basically the acts as the initiator of a new metastable thermodynamic state from a stable state. Further interphase transition occurs to a more stable state as the material tends to gain it. Nucleation is a common mechanism which generates first-order phase transitions, and it is the start of the process of forming a new thermodynamic phase.

The new fundamentals of ferromagnetism explain both magnetization and hysteresis. Magnetization is not a spin reorientation in the same crystal structure but requires changing the orientation of the spin carriers. It can be achieved by crystal rearrangement. These crystal rearrangements can occur by nucleation and propagation of interface. The formation of the “sigmoid” hysteresis loops is due to the increase in nucleation sites (crystal defects) per unit volume and the decrease in the amount of the original phase.

Nucleation lag is one of the causes of hysteresis during magnetic phase transitions. Nucleation demonstrated by structural rearrangement during magnetic phase transitions. This structural rearrangement causes magnetic ordering inside the material.[55] It was acknowledged that the "underlying physics behind the magnetocaloric effect is not yet completely understood".[57] Now the physical nature of a "giant" magnetocaloric effect is explained in terms of the new fundamentals of phase transitions, ferromagnetism, and ferroelectricity[56]. It is the latent heat of structural (nucleation-and- growth) phase transitions from a normal crystal state to the orientation-disordered crystal (ODC) state where the constituent particles are engaged in thermal rotation. The ferromagnetism of the material provides the capability to trigger the structural phase transition by application of magnetic field.[58]

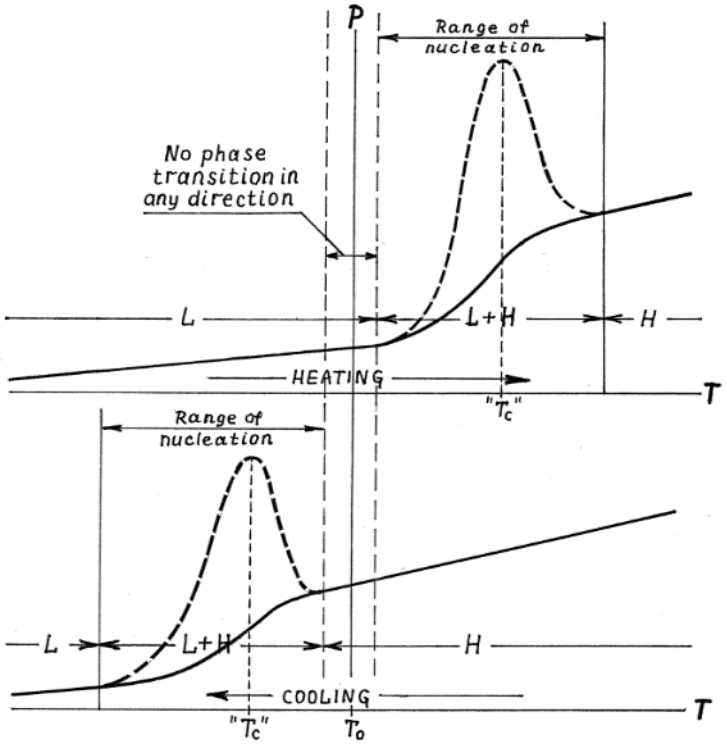

Fig. 2.9. A physical property P vs temperature T in the region of phase transition.

The "anomalous" peaks of a physical property P, believed to be a heat capacity or magnetization, reside in the ranges of transition (actually, ranges of nucleation). The “critical (Curie) point Tc” at the peak top is a subject of hysteresis, for there are two non-overlapping transition ranges, one above To - for heating, and the other below To - for cooling. In the adiabatic calorimetry these peaks are not a specific heat, but the latent heat of first order (nucleation and growth) phase transitions. A differential scanning calorimetry would reveal the peak in a cooling run looking downward, being exothermic. [58]

2.5 Magnetocaloric Materials from Published Reports:

The rare-earth metal Gd is considered the benchmark magnetocaloric material for room-temperature applications. The element was used as the refrigerant powering the first successful proof-of-principle refrigerator device. Temperature changes of 14 °K have been produced at room temperature by applying a 7T magnetic field to Gd metal. The Curie temperature of Gd is 293 °K, which makes Gd an ideal candidate for the working material in a room-temperature. Later the discovery of magnetocaloric materials $Gd_5(Si_2Ge_2)$ that exhibit giant magnetocaloric effect leads to a rapid interest in designing and developing magnetocaloric materials without critical or toxic elements to use in large quantities near room temperature. Rare earth elements

(Gd, La, Nd) and their alloys have been studied for magnetocaloric applications because of their great intrinsic magnetic property. Several promising materials have been developed, including FeRh, $Gd_5(Si_xGe_{4-x})$ alloys[49], $Tb_5Si_2Ge_2$[59] Heusler alloys with rare earth elements [60] $MnAs_{1-x}Sb_x$[61], $La(Fe_{1-x}Si_x)_{13}$ alloys and their hydrides $La(Fe_{1-x}Si_x)_{13}H_y$.[62] However, these materials mostly contain toxic and hazardous elements which hinder their long-term application in magnetic refrigeration.

Recent research has been sparked on replacing poisonous and expensive elements for commercial use of magnetocaloric materials. Many materials exhibit a large magnetocaloric effect but have one or more drawbacks. A large MCE was found in amorphous $Fe_{78-x}Cr_xSi_4Nb_5B_{12}Cu_1$ and $Fe_{73.5-x}Cr_xSi_{13.5}B_9Nb_3Cu_1$.[63, 64] Significant interest was devoted to the potentially viable MnMX (M = Co or Ni, X = Si or Ge) alloy, melt span Ni-Mn-Ga alloys and other materials.[65,66] Further development of viable magnetocaloric material from abundant and nontoxic elements is crucial for cooling technology.

Chapter 3: Experimental Method

The experimental work conducted for this thesis involves – sample preparation, determination of the crystalline structure and measurements of the magnetic and magnetocaloric properties of the samples. During these processes phase identification of the material is performed by SEM. A brief description of each of the steps is provided below.

3.1 Sample Preparation

Approximately 7.5g each of $Mn_{0.5}Fe_{0.5}Ni_{1-x}Co_xSi_{0.94}Al_{0.06}$ (x=0.025, 0.05, 0.075, 0.1), $Mn_{0.5}Fe_{0.5}Ni_{1-x}Cu_xSi_{0.94}Al_{0.06}$ (x=0.025, 0.05, 0.075, 0.1) samples were prepared in a high-purity argon atmosphere by standard arc melting technique. This technique is commonly used to prepare intermetallic alloys. After stoichiometric calculations, the constituent elements are weighed and placed on a copper hearth enclosed in a vacuum chamber. The chamber is evacuated several times and filled with argon gas each time. The melting is done in partial argon pressure. Heat is generated by the electric arc struck between a needle-like tungsten electrode and the copper hearth, which is then used to melt the elements to form an alloy. Cold water is circulated under the hearth and the electrode assembly during the whole melting process. Prior to melting, the Mn pieces were washed with diluted nitric acid to remove corrosion products and volatile impurities. To compensate for the loss of Mn at the time of melting, $\sim 5\ wt.\%$ extra Mn was added to the calculated stoichiometry of each sample. The ingots were flipped and melted three times to ensure chemical homogeneity and the mass loss after the melting was within 0.2%-0.5% for each sample. The arc-melted samples were further homogenized by vacuum suction-cast into cylindrical shapes, and half of each cylinder was wrapped in a tantalum foil and annealed for 7 days at 800°C in a partially evacuated/partially Ar-filled quartz ampule. $Mn_{0.5}Fe_{0.5}Ni_{0.0975}Co_{0.025}Si_{0.94}Al_{0.06}$ system is also measured in a powder form. Using liquid nitrogen on a ¾ ratio of the $7.5g$ of bulk sample. To ensure chemical homogeneity, the powdered sample was further annealed at 650 K and 800 K temperatures for 1 hour using the same procedure.

3.2 Structural Characterization

To investigate the crystal structure and the phase purity, room temperature x-ray diffraction (XRD) was collected using a Bruker D8 advance powder x-ray diffractometer with *Cu-K*α

radiation where the wavelength of the incident beam was 1.5Å. The diffraction patterns were further indexed using the FullProf software.[67]

3.2.1 Fundamental Principle of X-ray Diffraction Technique

X-ray is electromagnetic radiation with wavelengths between roughly 0.1Å and 100Å. X-ray diffraction is a common technique to determine the crystallographic structure of unknown crystalline materials. This tool is also used to identify phases by comparison with data from known structures and quantify changes in the cell parameters, orientation, crystallite size, and other structural parameters.

Crystals are regular arrays of atoms and thus can diffract light. When a crystalline sample is placed in the path of an x-ray beam, it will be scattered by the electrons of the atoms in the material. All the atoms in the path of the x-ray beam scatter x-rays and the scattered rays interfere, either destructively or constructively, with one another. This phenomenon is called x-ray diffraction. It was observed by two British Scientists William Lawrence Bragg and William Henry Bragg in 1913. From the observation, they demonstrated the relationship between x-ray wavelengths, incident angle, and distance between lattice planes, given by:

$$2dsin\theta = n\lambda$$

Where *d* is the interplanar spacing in the atomic lattice, *n* is the order of reflection, λ is the wavelength of the incident x-ray beam, and θ is the incident angle at which constructive interference occurs. The intensity of the reflected beam is collected at an angle of 2θ which is the angle measured between the source and detector. A schematic diagram of the Bragg law is given below:

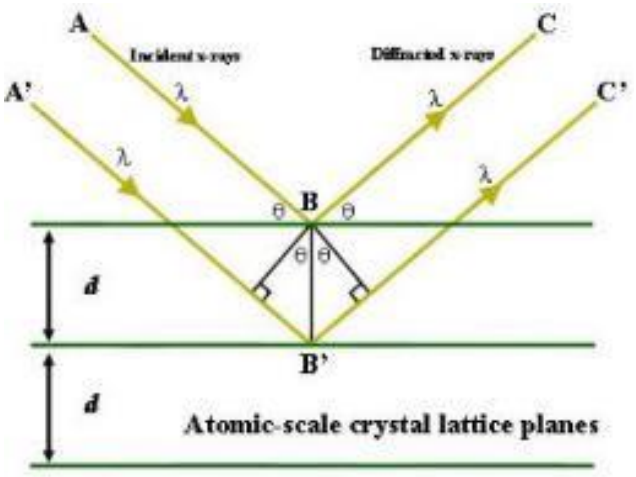

Fig. 3.1. A Schematic diagram represents Bragg's law of diffraction. Constructive interference occurs when the path length difference between ABC and A'B'C' is an integer multiple of wavelengths (λ).[68]

3.2.2 Production of x-ray

There are three basic elements in an x-ray diffractometer. These are an x-ray tube, sample holder, and x-ray detector. X-rays are commonly produced in x-ray tubes by accelerating electrons through a potential difference and directing them onto a target material. X-rays emit electrons from the cathode, accelerating with a high voltage and hitting an anode which is a metal target. X-ray is produced when electrons have sufficient energy to excite the inner shell electrons of the target material. X-ray spectra consist of the most common $K_{\alpha 1}$ and $K_{\alpha 2}$ and K_{β} transitions.[69] The wavelengths of the spectra are characterized by the different target materials. Commonly used target materials are Cu, Cr, Fe, and Mo. When x-rays are incident onto the sample, the sample and detector are rotated, and the intensity of the reflected x-rays is recorded. Constructive interference occurs due to the interaction of incident rays with the sample that satisfies the Bragg condition. A detector collects x-ray signals and converts the signal to a photon count rate.

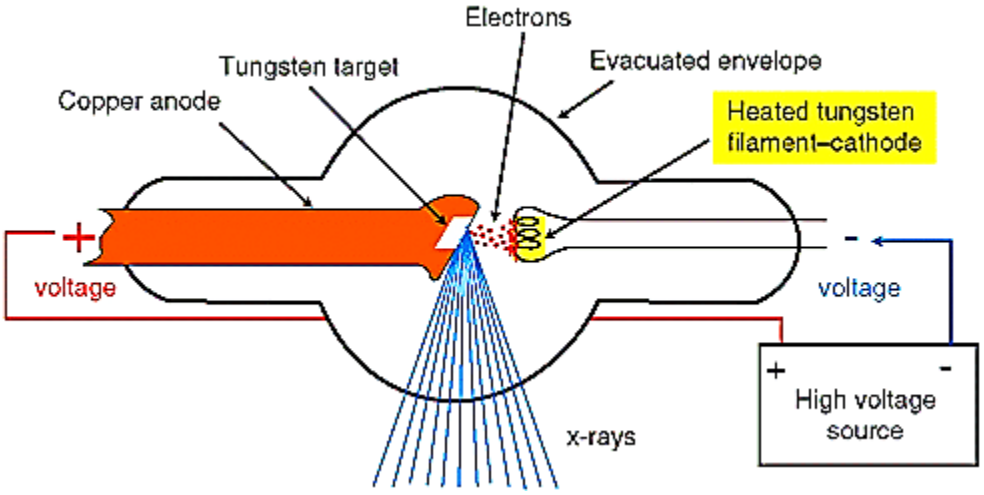

Fig. 3.2. Fundamental schematic structure of x-ray tube.

3.2.3 X-ray diffraction data measurement and analysis

The sample was cut into small portions and crushed into a fine powder with a mortar and pestle. The powder is then smeared on a rectangular glass and mounted in the sample holder before putting it on the x-ray diffractometer. Cu-Kα radiation with wavelength 1.5 Å is used to produce an x-ray and diffracted ray is collected by the detector. Each measurement took approximately 693 seconds to complete. Scanning the sample through a range of 2θ from 20° to 80° intensity of the reflected x-ray was recorded with an increment of 0.02.

Fig. 3.3. Bruker D8 advanced powder XRD at Miami University

The diffraction patterns were further indexed by FullProf software using the Rietveld refinement technique, which can provide Information about the crystal structure, lattice parameters, and crystalline phases of the sample. The crystalline phase of the samples is usually identified by matching the x-ray diffraction patterns with the expected patterns. Reference data can be obtained from the Crystallography Open Database which matches the intensity peak according to the distribution of atoms in the crystal structure.[70] For a sample with a hexagonal crystal structure, the relation between interplanar spacing d, lattice parameters (a, b, and c), Miller indices h, k, and l can be written as:

$$\frac{1}{d^2} = \frac{4}{3}\left(\frac{h^2 + hk + k^2}{a^2}\right) + \left(\frac{l^2}{c^2}\right)$$

Miller indices are defined as the reciprocals of the fractional intercepts which the plane makes with the crystallographic axes. The plane makes fractional intercepts of 1/h, 1/k, and 1/l with the axes a, b, and c, respectively. It was not calculated manually. The difference peak was matched with references data and miller index was determined using the published reference pattern.[70]

3.3 Compositional Characterization

3.3.1 Fundamentals of Scanning Electron Microscopy

The scanning electron microscopy (SEM) technique is widely used to examine the surface domain of a specific material. SEM can produce useful signals by scanning the surface of the sample to identify information about the single or multi-phase structure and chemical composition of the material. The SEM images included in this thesis were taken using a Zeiss Supra 35 VP FEG scanning electron microscope (SEM) at Miami University Center for Advanced Microscopy (CAMI). In SEM a focused beam of electrons is directed across the surface of the specimen. The electrons in the beam interact with the atom of the targeted sample, producing various signals that can be used to obtain information about the surface's topography and composition.[71] A schematic diagram of the SEM is given below.

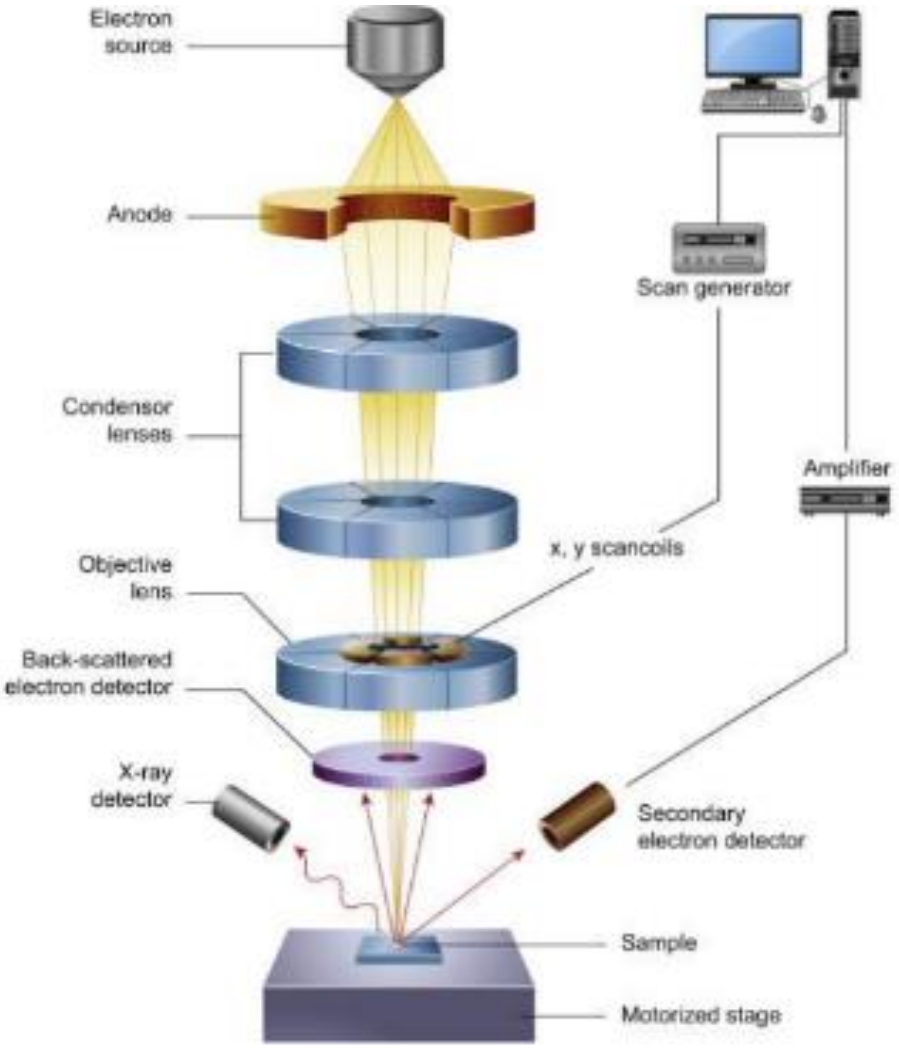

Fig. 3.4. Scheme of Scanning Electron Microscope (SEM) with the illustration of its components.

Fig. 3.5.The Scanning Electron Microscope (SEM) used for all the elemental analyses. It is housed in the Miami University Center for Advanced Microscopy and Imaging (CAMI), Zeiss Supra 35VP (variable pressure), X-ray fluorescence detector EDAX and HKL Electron Backscatter diffraction (EBSD) detector.

Electrons are generated at the top column by the electron source. Three different electron sources can be used in an SEM, which include thermionic filament, field emission gun (FEG), and Cerium hexaboride cathode (CeB6). These high-energy electrons are accelerated down the column that is under vacuum. The sample itself is mounted on a stage in the chamber area and electrons pass through a combination of lenses and apertures to produce a focused beam of electrons which then strikes the surface of the sample. Electromagnetic lenses are used to bend and control the path of the electrons. A group of condenser and objective lenses leads- main role to collimate and focus the beam onto the sample. Scanning coils are used to raster the beam onto the sample. This beam scanning enables getting information about a specific area on the sample to be collected. In many cases, apertures are combined with the lenses to control the size of the beam.

As the electron beam passes through the specimen, it is possible for the electrons to pass through the sample without interacting with the atoms of the target sample. The electrons may also undergo elastic or inelastic scattering and produce secondary electrons (SEs),

backscattered electrons (BSEs), and characteristic X-rays. These signals are collected by one or more detectors to form images which are then displayed on the computer screen. SEs typically originate near-surface regions of the specimen because of inelastic interactions between the electron beam and the sample. A Secondary Electron (SE) detector is placed at the side of the electron chamber, at an angle, to increase the efficiency of detecting secondary electrons which can provide more detailed information about the topography of the surface.

On the other hand, BSEs are generated from the deeper region of the sample as they have higher energy than SEs and are reflected after elastic interactions between the beam and the atoms. As the electrons within the beam collide with the atoms of the sample, a change in the electron's trajectory occurs. The intensity of the BSE signal is strongly related to the atomic number (Z) of the target sample.[72] The higher the atomic number, the brighter the material appears in the image. BSEs are typically detected by a BSE detector that is placed directly above the sample and provides information about the sample compositions. Each sample was polished before mounting using a polishing grinder and Sonicating in methanol to obtain high-quality SEM data.

3.3.2 Energy Dispersive Spectroscopy

Energy dispersive x-ray spectroscopy (EDS) is used to identify chemical elements present in a sample and estimate the relative proportion of these elements. According to the principle of Moseley's law, the frequency of the emitted electromagnetic spectrum is proportional to the atomic number of atoms.[73] When inelastic scattering occurs between the accelerated electrons and the atoms of the sample, inner shell electrons can eject from the atoms of a material. The electron with higher energy comes down to the lower energy level and releases the amount of access energy in the form of x-ray radiation (photon).

The wavelength of the x-ray is related to the difference in energy levels of electrons in different shells for a specific element in the periodic table. These characteristic x-rays from each element in the form of released energy help us to identify the element in the sample. The Zeiss Supra 35 is equipped with a Bruker Genesis EDS unit to detect these characteristics x-rays and the mapping of the elemental composition that can help to determine the accuracy of sample fabrication compared to the stoichiometric calculation.

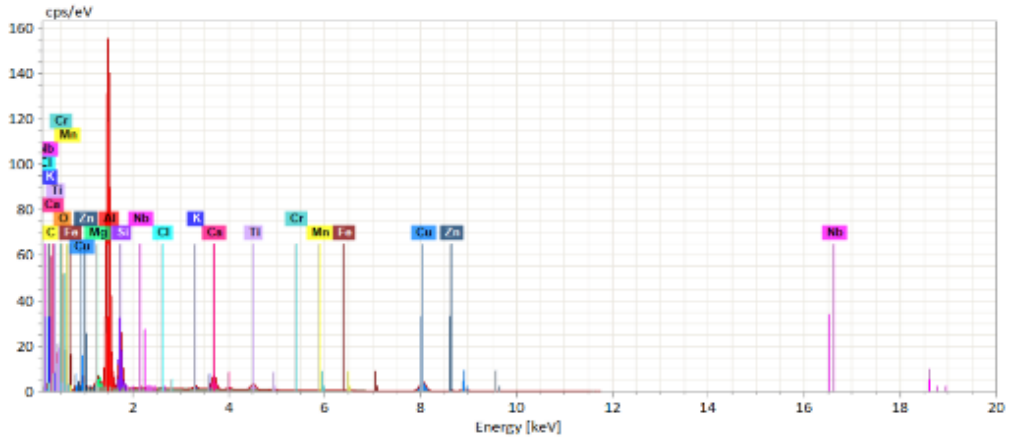

Fig. 3.6. Arbitrary EDS spectrum measuring photon counts with respect to the photon energy for a unknown sample.

3.3.3 Sample Fabrication for SEM

Surface roughness can act on the backscattered electron image and EDS analyses adversely. For more accurate surface details and compositional analysis from SEM micrograph, samples should be flat, and extremely clean. Unnecessary scratches, grains and debris can misinterpret the microstructure and composition of the specimen. Before mounting the sample, proper polishing is very important. To polish the sample, approximately 2 gm sample was cut with a diamond saw. First, a piece of wax was melted on top of the graphite plate. The sample was placed onto the wax and the graphite plate and cooled down for 5 minutes before mounting it into the goniometer. The portion of the sample was polished in a grinding machine using 120-grit sandpaper and 240-grit sandpaper respectively. Further polished with 1 µm diamond lapping film using 0.5 µm diamond spray and sample bath sonicated in methanol for 10-15 minutes.

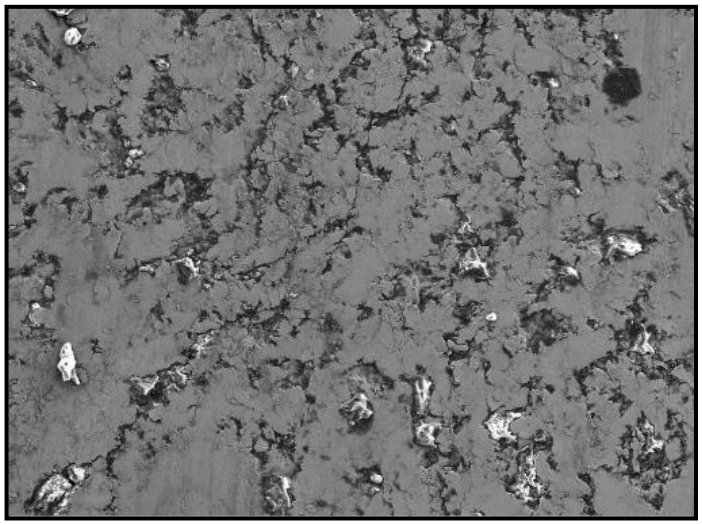

Fig. 3.7. SEM micrograph before polishing the $Mn_{0.5}Fe_{0.5}Ni_{1-x}Co_xSi_{0.94}Al_{0.06}$(x=0.05) sample.

3.4 Magnetic Measurement

The vibrating sample magnetometer (VSM) option on a Quantum Design Physical Property Measurement system (PPMS) was used for the magnetization measurements based on Faraday's Law of Induction. The magnetization as a function of temperature, M(T), measurements are being done between 50 K and 350 K for warming and cooling cycle at a constant magnetic field of 1 kOe or 2 kOe for each sample. Isothermal magnetization versus the field, M(H), measurements are being done at various temperatures in applied magnetic fields from 0 to 50 kOe. The phase transition temperature Tc are obtained from the M(T) data and the magnetic entropy changes, $\Delta S_M(T)$, for various field changes are evaluated from the M(H) data by using the following Maxwell relation:[74.]

$$\Delta S_M(T, \Delta H) = \int_{H_i}^{H_f} \left(\frac{\partial M\,(T,H)}{\partial T} \right)_H dH \ldots\ldots\ldots\ldots\ldots\ldots\ldots\ldots\ldots\ldots (3.3)$$

3.4.1 PPMS (Physical Property Measurement System)

Physical Property Measurement System (PPMS) instruments are widely used in scientific research and development. It can be used to perform magnetic, electro-transport, or thermo-electric measurements, or can be modified in the system to perform other laboratory experiments with high accuracy. The PPMS operates in the temperature range of 1.9 to 400 K and can supply magnetic fields up to ± 16 Tesla.[75]A superconducting coil is employed within the PPMS to produce this high magnetic field. Because of the high-temperature operating environment, liquid helium, and nitrogen supply are essential all the time for the proper operation of the PPMS.[76] The major component of PPMS is presented below:

Fig. 3.8. The Model 6000 PPMS Controller Device at Miami University.

3.4.2 Vibrating Sample Magnetometer (VSM)

One of the measurement options existing in PPMS is called the Vibrating Sample Magnetometer (VSM), which is a scientific tool able to measure the magnetic properties of materials based on Faraday's law of induction.[77]

3.4.2.1 Theory of Operation

According to Faraday's law, the induced voltage in a circuit is directly proportional to the changing magnetic field in the circuit. VSM measures the value of magnetization with respect to temperature or applied field. When the sample is placed inside the VSM, it vibrates perpendicularly to the uniform external magnetic field which is produced by the superconducting coil. As the sample vibrates, it moves between the center points of a two-segment pickup coil which is found in the sample region. The magnetic dipole moment of the sample creates a magnetic field that will change with time. As the sample moves up and down, it will generate a varying magnetic flux.[78] From Faraday's law, an induced emf is exerted on the pickup coils by the magnetic flux and can be expressed by the equation:

$$V = \frac{d\varphi_M}{dt} = \frac{d\varphi_M}{dz} \times \frac{dz}{dt}$$

φ_M represents the magnetic flux, z is the vertical distance between the sample and the coil, and t is the time. This induced voltage can be converted to the magnetization value. The sample oscillates sinusoidally at a frequency of 40 Hz in the VSM. For a sinusoidally oscillated sample, the induced voltage can be expressed as:

$$V = 2\pi f\ C\ m\ A \sin(2\pi f t)$$

C is the coupling constant, m is the DC magnetic moment, A is the amplitude of the oscillation and f is the frequency of the oscillation. The center of oscillation is positioned at the vertical center of pickup coil. The sample which is fixed to the sample rod vibrates with a given frequency and amplitude. It is centered between the two pole pieces of an electromagnet or superconducting magnet that generates a magnetic field of high homogeneity. Stationary pickup coils are mounted on the poles of the magnet. Hence, the change in magnetic flux originating from the vertical movement of the magnetized sample induces a voltage. The voltage induced in the pickup coil is amplified and lock-in detected in the VSM detection

module. The coefficient of the sinusoidal voltage response from the detection coil measures the magnetic moment of the sample[32] and magnitude of the magnetic field is coming from a gaussmeter. From VSM information regarding phase transitions and the magnetic nature, and the magnetocaloric effects of the compounds could be obtained.

3.4.2.2 Components of VSM

The VSM option consists of a vibrational head (linear motor transport) for vibrating the sample, sensing or pickup coils for detection, electronics for driving the linear motor and detecting the response from the coils, and data acquisition software.[78]

Pickup Coils: The VSM has 3 different known configurations for detection coils named as: 1) Foner, 2) Mallison, and 3) Bowden. The Foner configuration is based on two pick-up coils connected in series to obtain a net output signal. This configuration eliminates the background noise caused by the instability of the magnetic field or mechanical vibrations of the electromagnet and coil systems. The Mallison configuration has four pick-up coils in series with their axes parallel to the x-axis. The Mallinson coil set has higher inherent sensitivity to magnetic samples because it has a very low signal to noise ratio. The signals from the coils, however, have a large dependence on the sample's position. This is due to the placement of the coils directly parallel to the field. As the sample moves towards or away from one of the coils the signals will increase or decrease. The Bowden configuration consists of eight pick-up coils in series with their axes parallel to the y-axis. The pick-up coils are assembled either parallel or perpendicular to the direction of the magnetic field generated from the electromagnet poles. The vertical movement of the magnetized sample produces a change in the magnetic flux that induces a voltage V in the detection coils.

Vibrational Head: The vibrating head provides a vibration of constant frequency and amplitude as a function of time. The amplitude of vibration should be sufficiently small to ensure that a sample is subjected to a homogeneous magnetic field, and it should be less than the pickup coil diameter. The head should provide a stable reference signal for lock-in detection of the signal induced in the pickup coils. The head should be either passively or dynamically decoupled from the electromagnet and coils to minimize induced coherent noise in the coils due to vibration coupling.

VSM Electronics: A VSM requires gaussmeter for closed loop field control, electronics to drive the VSM head, a lock-in amplifier to provide the head with an AC reference signal and to measure the induced voltage in the pickup coils, and a temperature controller if the VSM is equipped with variable temperature apparatus. MultiVu software can make automated sequence commands and control the system parameters.

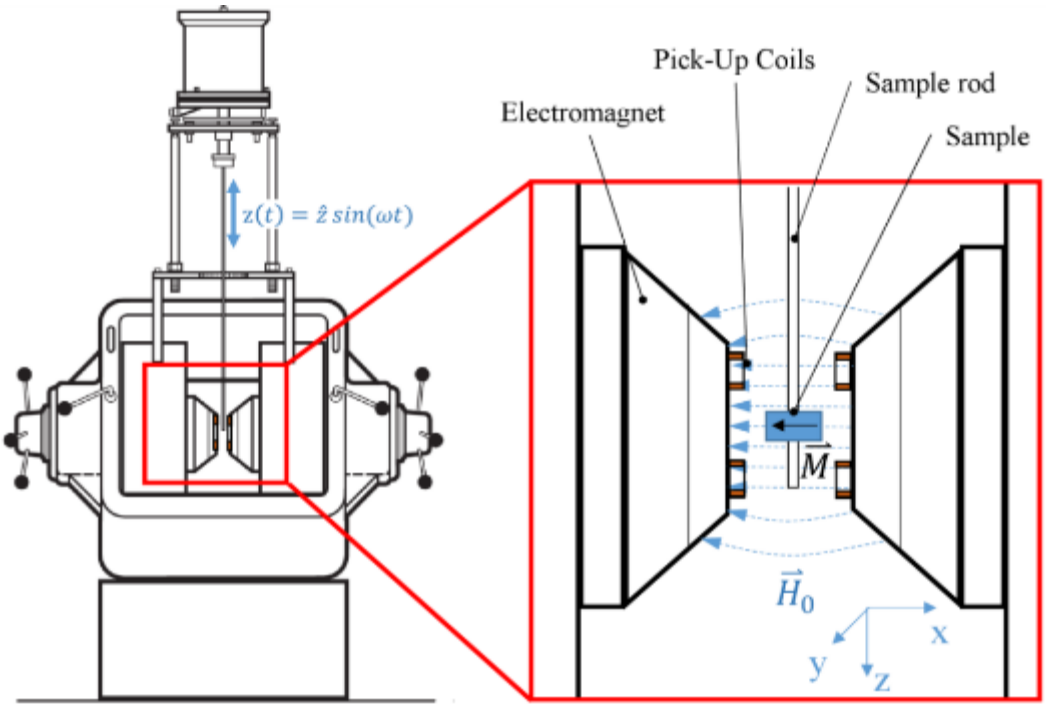

Fig. 3.9. Schematic diagram of VSM module of PPMS.

Chapter 4: Results and Discussions

4.1 Structural Characterization and Compositional Analysis

A complete list of samples that are being investigated for this thesis is provided in Table 2. Room temperature XRD was performed for the $Mn_{0.5}Fe_{0.5}Ni_{1-x}Co_xSi_{0.94}Al_{0.06}$ and $Mn_{0.5}Fe_{0.5}Ni_{1-x}Cu_xSi_{0.94}Al_{0.06}$ systems to determine the phase purity and the crystalline parameter like lattice constant, cell volume. The XRD data of all samples were refined by the Rietveld refinements using the FullProf software. The composition analysis and identification of phases were done by scanning electron microscope (SEM), and energy-dispersive x-ray spectroscopy (EDS).

4.1.1 Structural Characterization

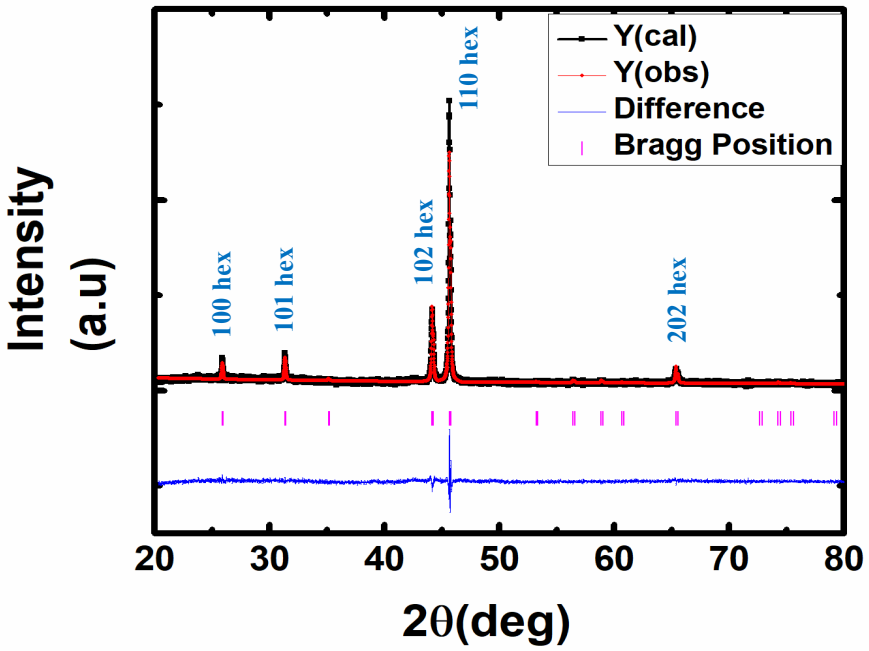

Fig. 4.1. Room temperature XRD refinement data for as-cast $Mn_{0.5}Fe_{0.5}Ni_{0.975}Co_{0.025}Si_{0.94}Al_{0.06}$ compound. The pink bars indicate the Bragg position, and the blue line represents the difference between the calculated and observed value. ($\chi^2 = 1.13$).

The diffraction data for all the other samples in the series (x =0.025 and 0.05, 0.075, 0.1), both as-cast and annealed, showed similar structure as shown in Fig. 4.2 and Fig. 4.3 respectively. No other phases were observed in the XRD data. The lattice parameters marginally varied with

x from *a=b= 3.9719* and *c=5.1045* Å (*x* =0.025) to *a=b=3.9728* Å to *c=5.1039* Å (*x* =0.05) for the as-cast samples. In the case of annealed samples, lattice parameters changed with *x* from *a = b = 3.9677* Å and *c = 5.0966* Å (*x* = 0.025) to *a = b = 3.9742* Å and *c = 5.1057* Å (*x* = 0.05). The values are comparable to the published literature data.[74] Considering the coordination number, CN = 12, the atomic radii for Co and Ni are 1.252 Å and 1.246 Å, respectively.[79,80,81] The increase of lattice parameters with increasing *x* may be attributed to the larger atomic radius of Co. The ratio of the *c/a* slightly decreases with increasing *x* indicates that Ni_2In hexagonal structure is stabilized in the sample at room temperature.[82] The value of the unit cell and lattice parameter a, b, c with changing *x* is given in Table 1.

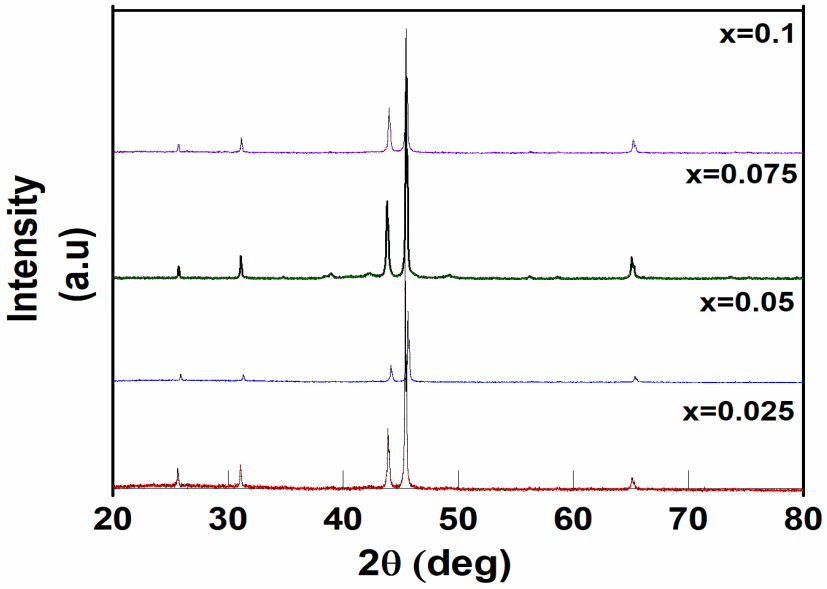

Fig. 4.2. XRD patterns for as-cast sample.

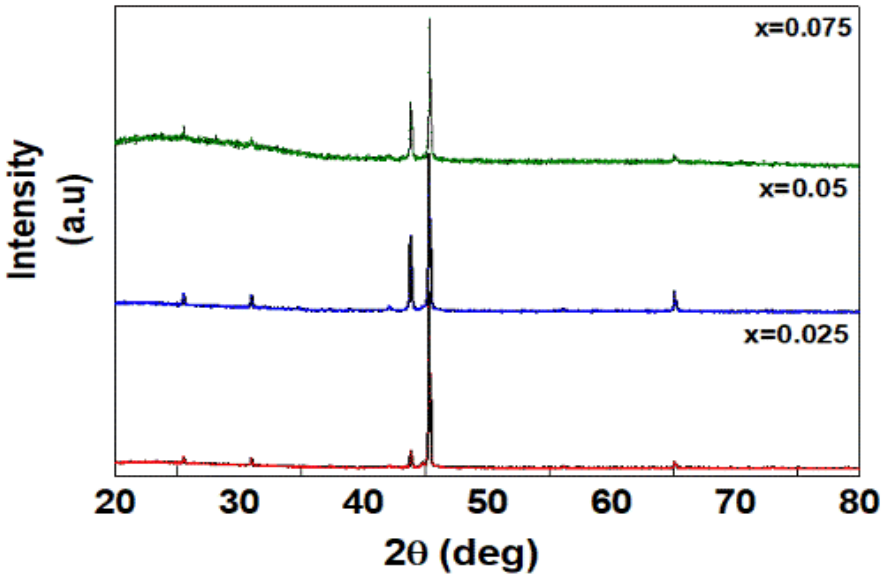

Fig. 4.3. XRD patterns for annealed sample

Cu-doped (x = 0.025 and 0.1) compound exhibited the same structure (space group P63/mmc). For this system, the lattice parameter changed from $a=b$=3.9722 Å and c=5.1054 Å (x = 0.025) to $a=b$=3.9661 Å and c=5.0953 Å (x = 0.1). The marginal change in lattice parameters with x can be attributed to the similarity between the radius of Cu (1.278 Å) and Ni (1.246 Å) atom.[79] The ratio of the c/a is slightly decreased with increasing x which determines that Ni_2In type hexagonal structure is stabilized.

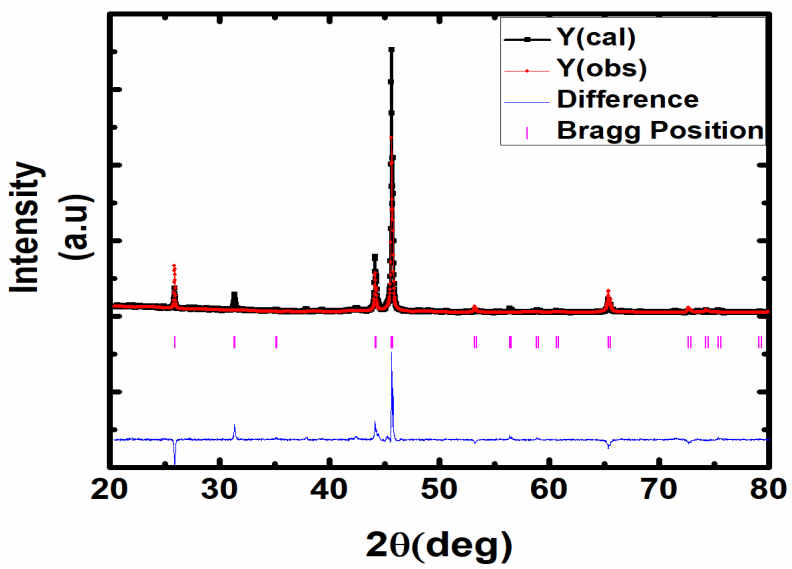

Fig. 4.4. Diffraction pattern for the as-cast $Mn_{0.5}Fe_{0.5}Ni_{0.975}Cu_{0.025}Si_{0.94}Al_{0.06}$ compound. The pink bars indicate the Bragg position and blue line represent the difference between calculated and observed value ($\chi 2$ =3.93).

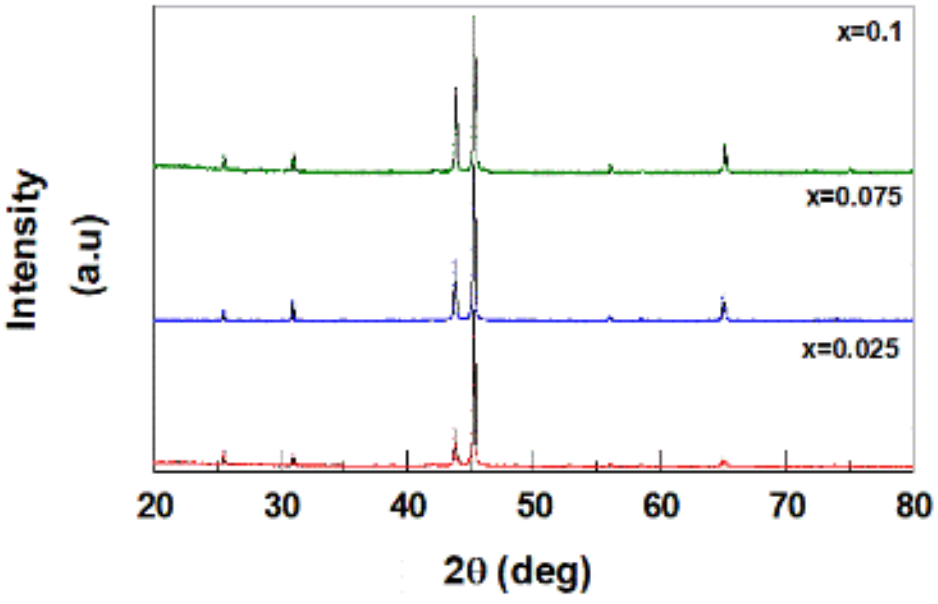

Fig. 4.5. Diffraction patterns for the $Mn_{0.5}Fe_{0.5}Ni_{1-x}Cu_xSi_{0.94}Al_{0.06}$ system.

Table 1: Lattice Parameter and Unit cell volume of $Mn_{0.5}Fe_{0.5}Ni_{1-x}Co_xSi_{0.94}Al_{0.06}$ (x=0.025, 0.05, 0.075) and $Mn_{0.5}Fe_{0.5}Ni_{1-x}Cu_xSi_{0.94}Al_{0.06}$ (x=0.025, 0.1) samples.

Sample	Lattice Parameter			Volume
	a	b	c	
As-cast $Mn_{0.5}Fe_{0.5}Ni_{0.975}\ Co_{0.025}Si_{0.94}Al_{0.06}$	3.9719 Å	3.9719 Å	5.1045 Å	69.7398 $(Å)^3$
As-cast $Mn_{0.5}Fe_{0.5}Ni_{0.95}\ Co_{0.05}Si_{0.94}Al_{0.06}$	3.2728 Å	3.2728 Å	5.1039 Å	69.7618 $(Å)^3$
As-cast $Mn_{0.5}Fe_{0.5}Ni_{0.925}\ Co_{0.075}Si_{0.94}Al_{0.06}$	3.9714 Å	3.9714 Å	5.1313 Å	70.0864$(Å)^3$
Annealed $Mn_{0.5}Fe_{0.5}Ni_{0.975}\ Co_{0.025}Si_{0.94}Al_{0.06}$	3.9677 Å	3.9677 Å	5.0966 Å	69.4561 $(Å)^3$
Annealed $Mn_{0.5}Fe_{0.5}Ni_{0.95}\ Co_{0.05}Si_{0.94}Al_{0.06}$	3.9742 Å	3.9742 Å	5.1057 Å	69.8361 $(Å)^3$
As-cast $Mn_{0.5}Fe_{0.5}Ni_{0.975}\ Cu_{0.025}Si_{0.94}Al_{0.06}$	3.9722 Å	3.9722 Å	5.1054 Å	69.7645 $(Å)^3$
As-cast $Mn_{0.5}Fe_{0.5}Ni_{0.9}\ Cu_{0.1}Si_{0.94}Al_{0.06}$	3.9661 Å	3.9661 Å	5.0953 Å	69.4113 $(Å)^3$

4.1.2 Compositional Analysis

To analysis the microstructure and composition of the constituent elements SEM micrograph was taken for $Mn_{0.5}Fe_{0.5}Ni_{1-x}Co_xSi_{0.94}Al_{0.06}$ and $Mn_{0.5}Fe_{0.5}Ni_{1-x}Cu_xSi_{0.94}Al_{0.06}$ systems. The images were collected using SE2 and back scattered (BSD) detector. The sample was scanned in 500 x and 2000 x magnification with 30 μm aperture. For all samples, the SEM micrographs confirmed that no secondary phases were present in the sample. In Fig. 4.6(a) and Fig. 4.6(b). show as cast and annealed $Mn_{0.5}Fe_{0.5}Ni_{0.95}Co_{0.05}Si_{0.94}Al_{0.06}$ sample after polishing. From SE2 image fewer patches of grain were observed in the sample. Black spots assumed to be pits but mostly debris due to residual from cutting and polishing.

In Fig. 4.7(a) and Fig. 4.7(b) represent the backscattered image of as-cast $Mn_{0.5}Fe_{0.5}Ni_{1-x}Cu_xSi_{0.94}Al_{0.06}$ sample after polishing (x = 0.025 and x = 0.1). Where all the samples are chemically homogenous. Energy dispersive spectroscopy (EDS) was used for compositional analysis. The extremely specific elemental composition data across an area of a sample is measured by EDS mapping. Characteristic photons for each element on the periodic table with specific energies are used to calculate fractional percentages of each element in a material and estimate the composition of a material.

EDS spectrum was measured for as cast $Mn_{0.5}Fe_{0.5}Ni_{1-x}Cu_xSi_{0.94}Al_{0.06}$ and constituent elements are found in a satisfactory ratio for each element. EDS spectrum is shown in Fig. 4.8

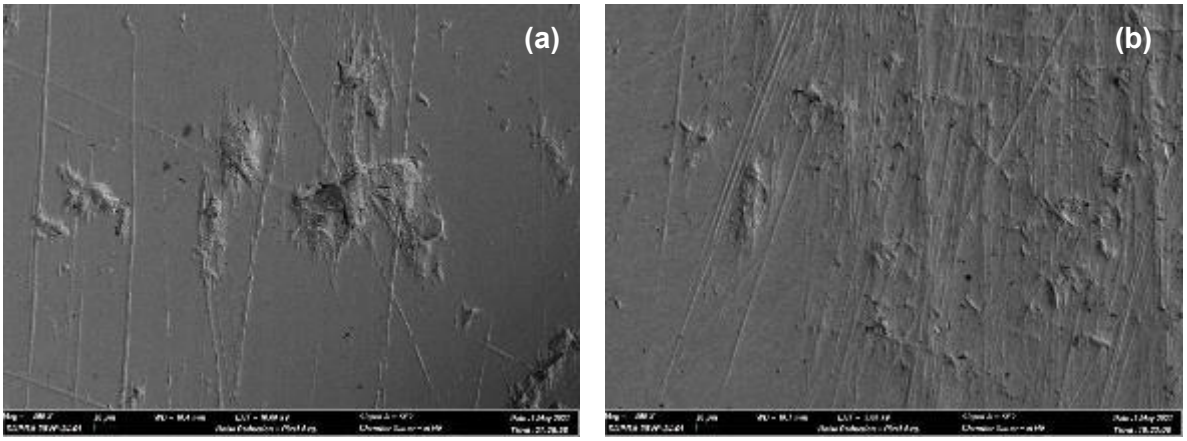

Fig. 4.6. Room temperature SE2 image for (a) as cast and (b) annealed sample $Mn_{0.5}Fe_{0.5}Ni_{1-x}Co_xSi_{0.94}Al_{0.06}$(x=0.05) sample.

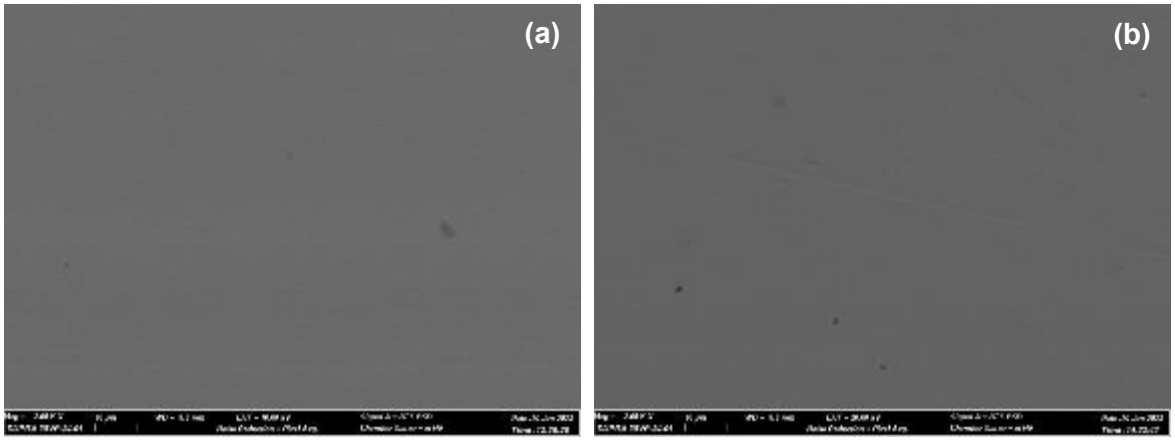

Fig. 4.7. Room temperature backscattered SEM image for as-cast $Mn_{0.5}Fe_{0.5}Ni_{1-x}Cu_xSi_{0.94}Al_{0.06}$ (a)x=0.025, and (b) x=0.1 sample.

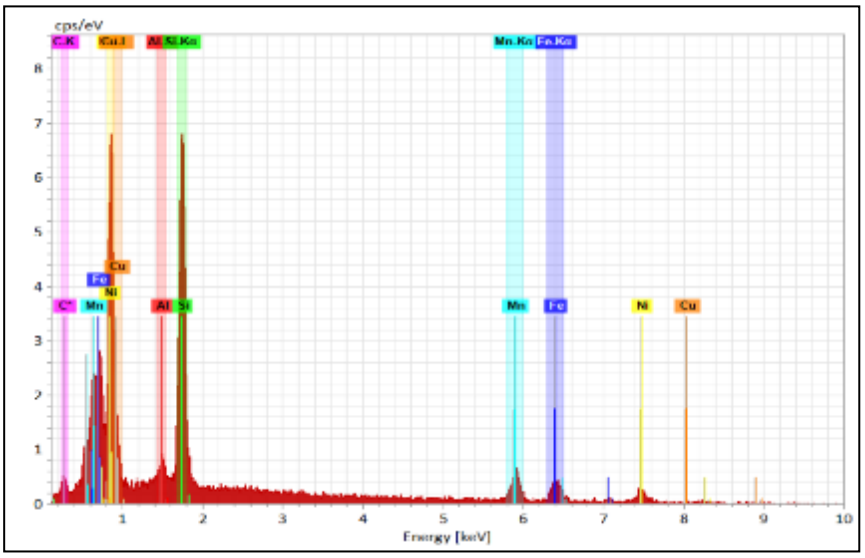

Fig. 4.8. EDS spectrum for as-cast $Mn_{0.5}Fe_{0.5}Ni_{1-x}Cu_xSi_{0.94}Al_{0.06}$(x= 0.1)

4.2 Magnetic Measurement

4.2.1 Temperature Dependence Magnetization M(T)

Fig. 4.9 and Fig. 4.10. show the M(T) data measured as a function of temperature for the bulk as-cast and annealed $Mn_{0.5}Fe_{0.5}Ni_{1-x}Co_xSi_{0.94}Al_{0.06}$ (x=0.025 and 0.05) samples respectively. All the measurements were done from 5K to 350K during the heating and cooling cycles at a constant magnetic field of 2 kOe. For all samples, the sharp fall of magnetization indicated a single ferromagnetic phase transition accompanied by a thermomagnetic hysteresis. The phase transition temperature Tc was determined from the derivative of the M(T) graph. In the as-cast sample for x = 0.025, the transition occurred at 227 K (warming) and 194 K (cooling), showing a thermal hysteresis of 33 K. The transition temperatures for the annealed sample increased to 258 K (warming) and 232 K (cooling) showing a thermal hysteresis of 26 K. Annealing the samples not only increased the transition temperatures but also reduced thermal hysteresis by 7 K. Similar behavior was observed for the as-cast and annealed samples with x = 0.05. For warming, the transition temperature increased from 236 K (as cast) to 256 K (annealed), and for cooling the temperature increased from 206 K to 220 K. Annealing caused thermal hysteresis to increase by 6 K for the sample with x = 0.05. According to the data, the phase transition Tc is not linearly dependent on the concentration of Co during the warming and cooling process which is shown in Fig. 4.11 and Fig. 4.12. The transition temperatures for all the samples were lower than the value reported for $Mn_{0.5}Fe_{0.5}NiSi_{0.94}Al_{0.06}$.[83] The increase of the transition temperatures due to annealing is not uncommon and has been reported for other Mn-Fe-based intermetallic systems.[84] For all samples, the thermal hysteresis during the heating and cooling cycle indicates that the sample exhibit first order phase transition (FOMPT). The value of the Tc with x is represented for all the samples in Table 2. Fig. 4.13 represents the M(T) data measured as a function of temperature for the powder $Mn_{0.5}Fe_{0.5}Ni_{0.975}Co_{0.025}Si_{0.94}Al_{0.06}$ (as-cast and annealed) sample which was measured at a constant magnetic field of 1 kOe from 5 K to 350 K temperature for both warming and cooling cycle. For both as-cast and annealed samples, Tc was increased in powder form compared to the bulk system (x=0.025) showing thermal hysteresis of 24 K for both cases. In the case of the as-cast sample, phase transition temperature was increased from 230 K to 254 K during the cooling and heating cycle. While for annealed sample Tc fluctuated between 242 K to 266 K in cooling and warming cycle.

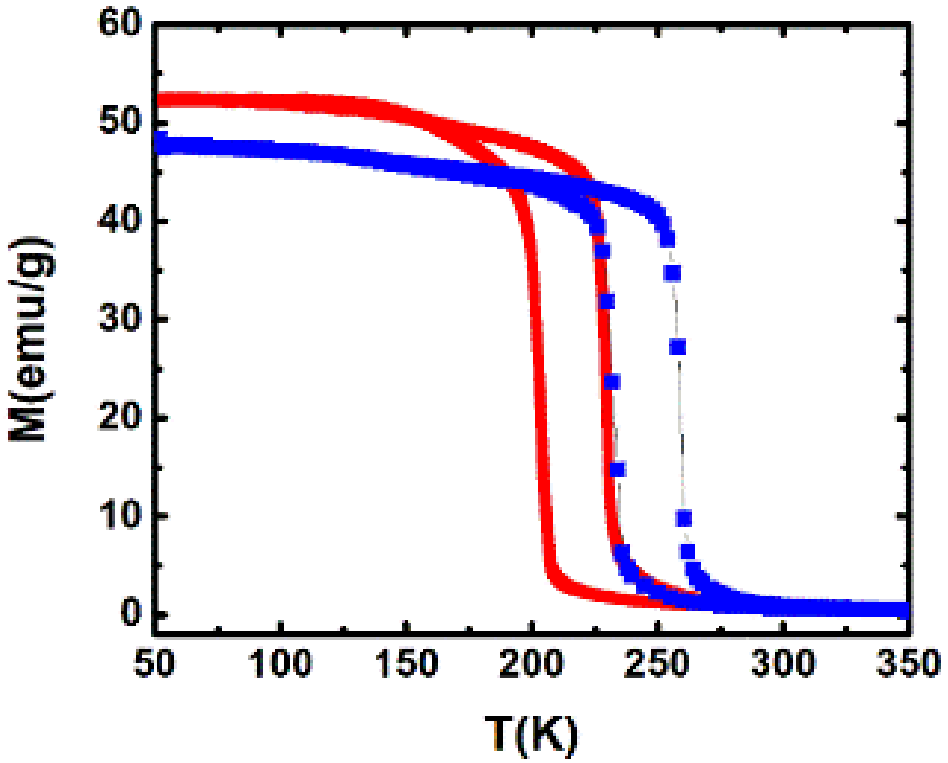

Fig. 4.9. Temperature dependence of magnetization for $Mn_{0.5}Fe_{0.5}Ni_{0.975}Co_{0.025}Si_{0.94}Al_{0.06}$ measured at a magnetic field of 2 kOe.

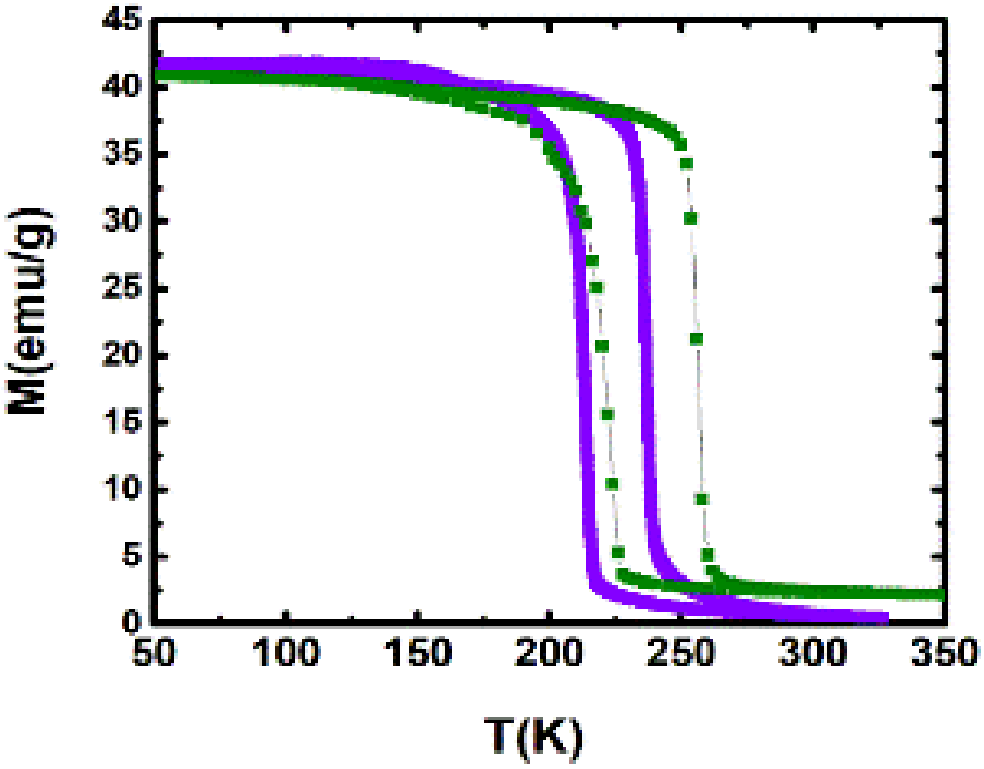

Fig. 4.10. Temperature dependence of magnetization for $Mn_{0.5}Fe_{0.5}Ni_{0.95}Co_{0.05}Si_{0.94}Al_{0.06}$ measured at a magnetic field of 2 kOe.

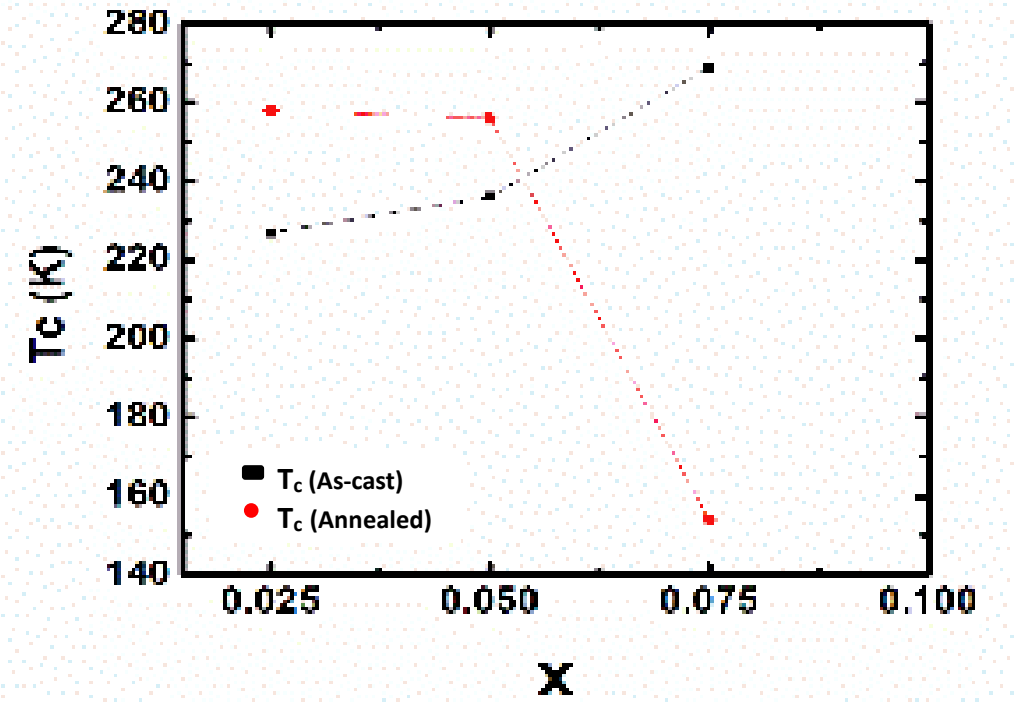

Fig. 4.11. Co concentration (x) dependence of Tc during the heating cycle. The black and red lines represent the as-cast and annealed $Mn_{0.5}Fe_{0.5}Ni_{1-x}Co_xSi_{0.94}Al_{0.06}$ (x=0.025, 0.05, 0.075) sample respectively.

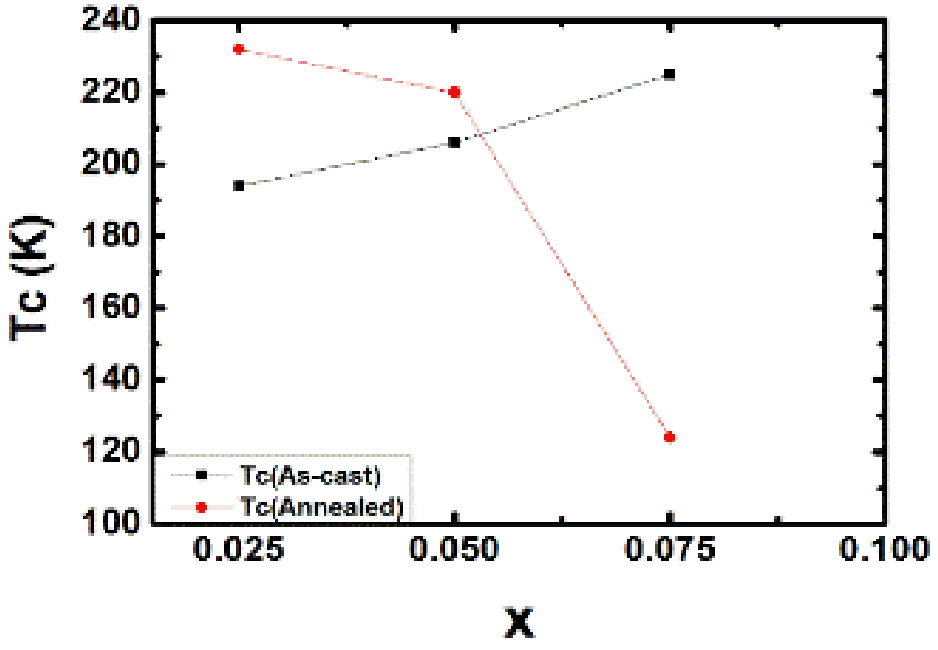

Fig. 4.12. Co concentration (x) dependence of Tc during the cooling cycle. The black and red lines represent the as-cast and annealed $Mn_{0.5}Fe_{0.5}Ni_{1-x}Co_xSi_{0.94}Al_{0.06}$ (x=0.025, 0.05, 0.075) sample respectively.

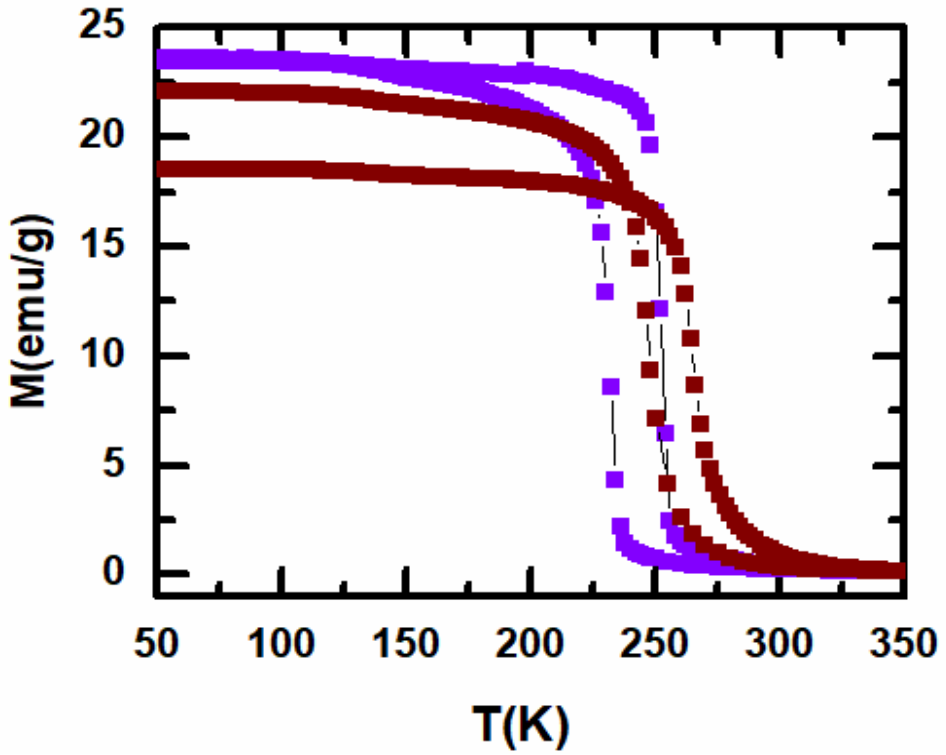

Fig. 4.13. Temperature dependence of magnetization for powder as-cast and annealed $Mn_{0.5}Fe_{0.5}Ni_{0.975}Co_{0.25}Si_{0.94}Al_{0.06}$ measured at a magnetic field of 1 kOe.

Magnetization data with respect to temperature was measured for the as-cast $Mn_{0.5}Fe_{0.5}Ni_{1-x}Cu_xSi_{0.94}Al_{0.06}$ (x = 0.025, 0.075, 0.1) sample using the same protocol. For a constant magnetic field of 1 kOe, magnetization was measured from 5 K to 350 K temperature both increasing and decreasing cycle. For all samples, M(T) data indicated a first order phase transition accompanied by a thermal hysteresis. In the as-cast sample for x = 0.025, the transition occurred at 216 K (warming) and 192 K (cooling), showing a thermal hysteresis of 24 K.

The transition temperatures for the (x=0.1) sample decreased to 196 K (warming) and 174 K (cooling) showing a thermal hysteresis of 22 K. Fig. 4.14. represents magnetization data as a function of temperature for $Mn_{0.5}Fe_{0.5}Ni_{1-x}Cu_xSi_{0.94}Al_{0.06}$ (x=0.025, 0.1) sample indicating Cu substitution reduced the thermal hysteresis of the system. Based on the measurement, the phase transition temperature Tc is linearly dependent on the concentration of Cu both warming and cooling process and reduces with the increment of Cu concentration, which is shown in Fig. 4.15.

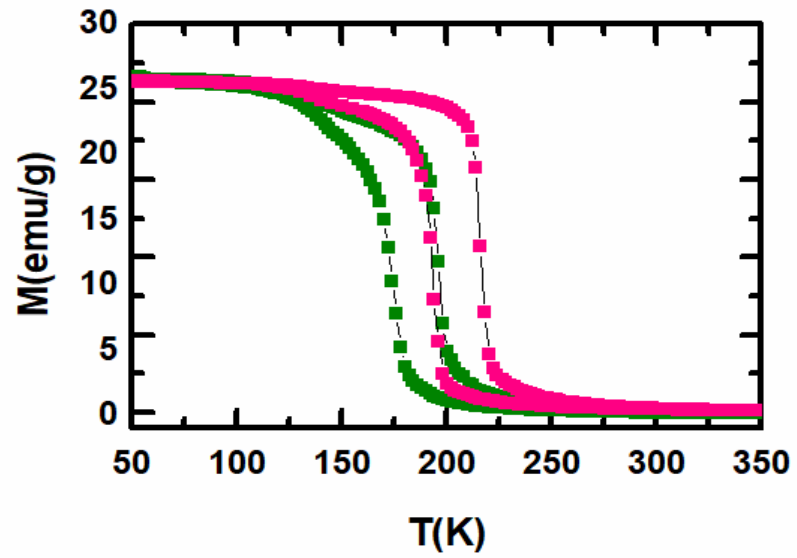

Fig. 4.14. Temperature dependence of magnetization for as-cast $Mn_{0.5}Fe_{0.5}Ni_{1-x}Cu_xSi_{0.94}Al_{0.06}$ (x = 0.025, 0.1) measured at a magnetic field of 1 kOe.

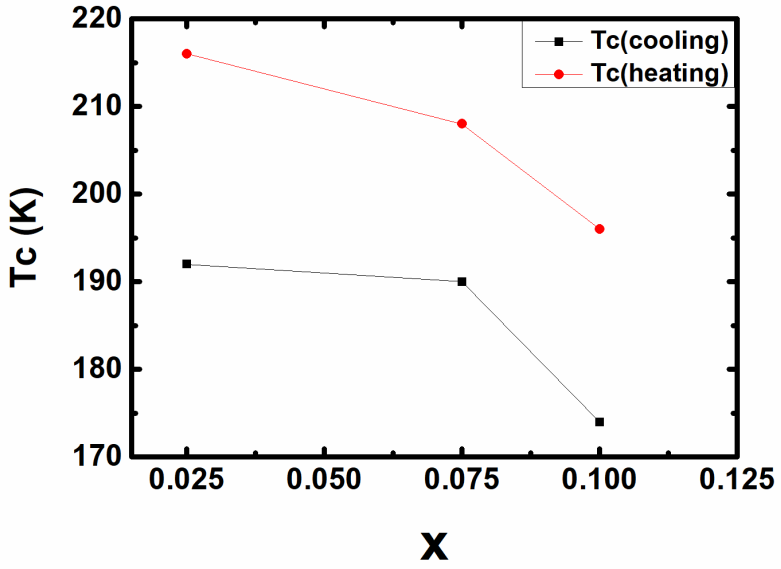

Fig. 4.15. Cu concentration (x) dependence of Tc. The black and red lines represent the as-cast $Mn_{0.5}Fe_{0.5}Ni_{1-x}Cu_xSi_{0.94}Al_{0.06}$ (x=0.025, 0.075, 0.1) sample during cooling and heating cycle respectively.

4.2.2 Magnetic field dependence magnetization M(H)

Isothermal magnetization M(H) data was obtained for the $Mn_{0.5}Fe_{0.5}Ni_{1-x}Co_xSi_{0.94}Al_{0.06}$ (x = 0.025, 0.05, 0.075) samples as a function of applied magnetic field H. Magnetic response for the as-cast and annealed *x* = 0.025 samples are shown in Fig. 4.16(a) and Fig. 4.16(b). The data was obtained while warming at temperatures from 176 K to 240 K for as-cast sample and 200 K to 295 K for annealed sample in 5 K (below the transition temperature) and 2 K (near the transition temperature) increments. For each temperature, the data showed typical

ferromagnetic behavior and did not show any field-induced metamagnetic phase transition for both samples. A magnetization of ~ 74 emu/g (at 50 kOe) was observed for as-cast sample at 176 K that slowly decreased with increasing temperature where saturation magnetization was ~ 43 emu/g for annealed sample at 200 K temperature.

The M(H) curves in as-cast sample were measured from 220 K to 226 K as a function of increasing and decreasing field. As can be clearly seen, the data showed no magnetic hysteresis, which is one of the desired criteria for an ideal magnetic refrigerant. It is interesting to note that the Co-doped $(Mn_{0.6}Fe_{0.4})$ $(Ni_{1-x}Co_x)$ Si system reported by Panda *et al.*, showed a large magnetic hysteresis.[16] M(H) value didn't change linearly by the increment of x. For an annealed x=0.05 sample, Magnetization data was measured from 180 K to 280 K during heating and 204 K to 280 K during cooling cycle under the magnetic field up to 50 kOe which was shown in Fig . 4.17(a) and Fig. 4.17(b). Saturation magnetization was obtained ~ 68 emu/g at 180 K at heating cycle and ~ 64 emu/g during cooling cycle. Which was decreased with increasing temperature indicating the ferromagnetic behavior for both samples Field-induced hysteresis was obtained with the increasing and decreasing of the magnetic field during the cooling cycle, indicating the first-order nature of field-induced phase transition. However, in the case of heating the magnetization curve completely coincided leaving no magnetic hysteresis.

Near the magnetic phase transition, field induced metamagnetic behavior is observed in the M(H) graph during the cooling process in the annealed x=0.05 sample it is shown in Fig. 4.18. From the magnetization curve at 238 K to 240 K, the phase transformation can be characterized by the hysteresis between magnetization and demagnetization process.

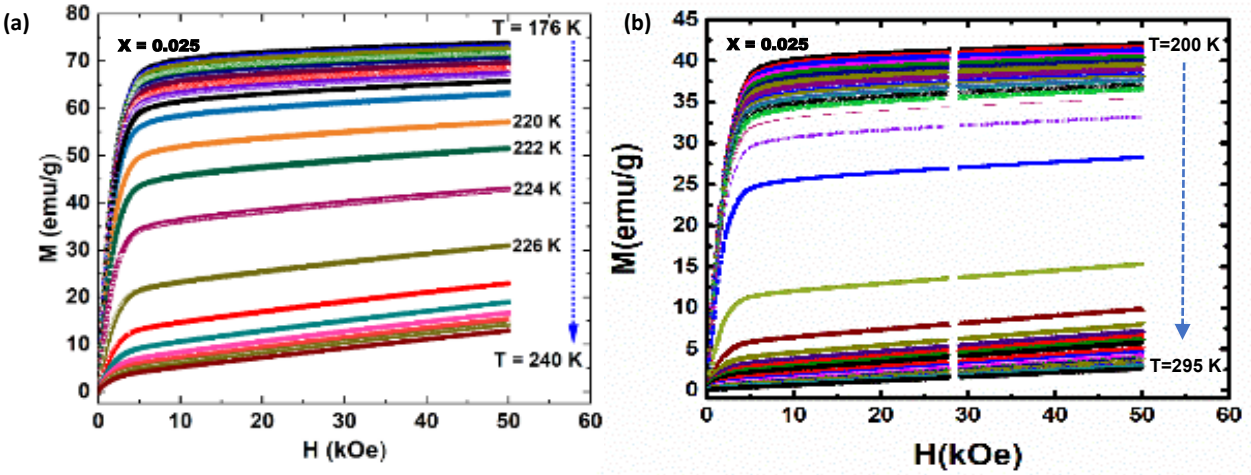

Fig. 4.16. Magnetization versus field for (a) as-cast and (b) annealed $Mn_{0.5}Fe_{0.5}Ni_{1-x}Co_xSi_{0.94}Al_{0.06}$ (x=0.025) obtained at various temperatures near the first order phase transition.

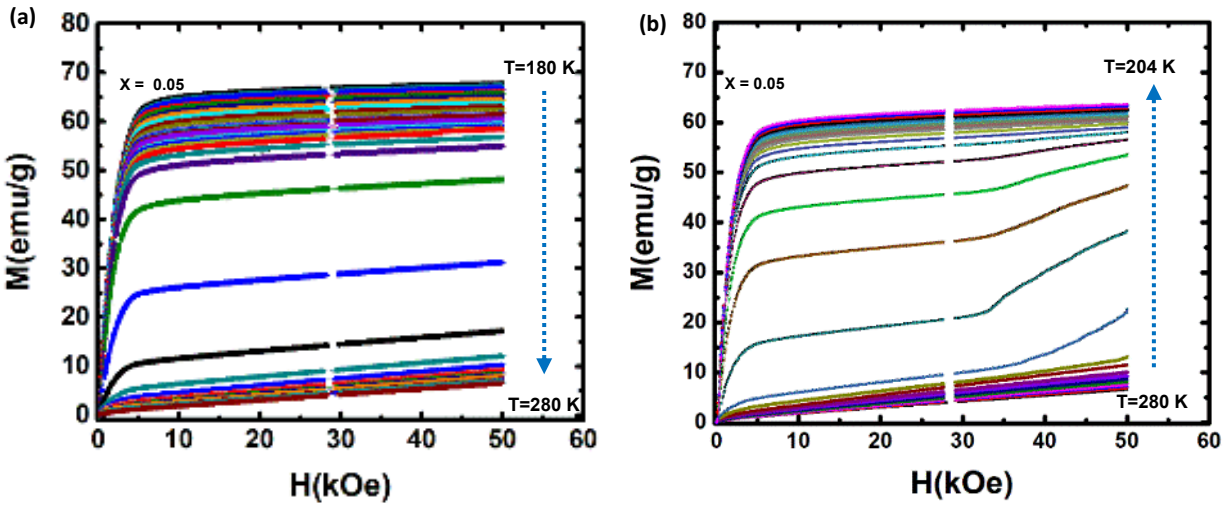

Fig. 4.17. Magnetization versus field for annealed $Mn_{0.5}Fe_{0.5}Ni_{1-x}Co_xSi_{0.94}Al_{0.06}$ (x=0.05) obtained at various temperatures near the first order phase transition for (a) heating and (b) cooling cycle respectively.

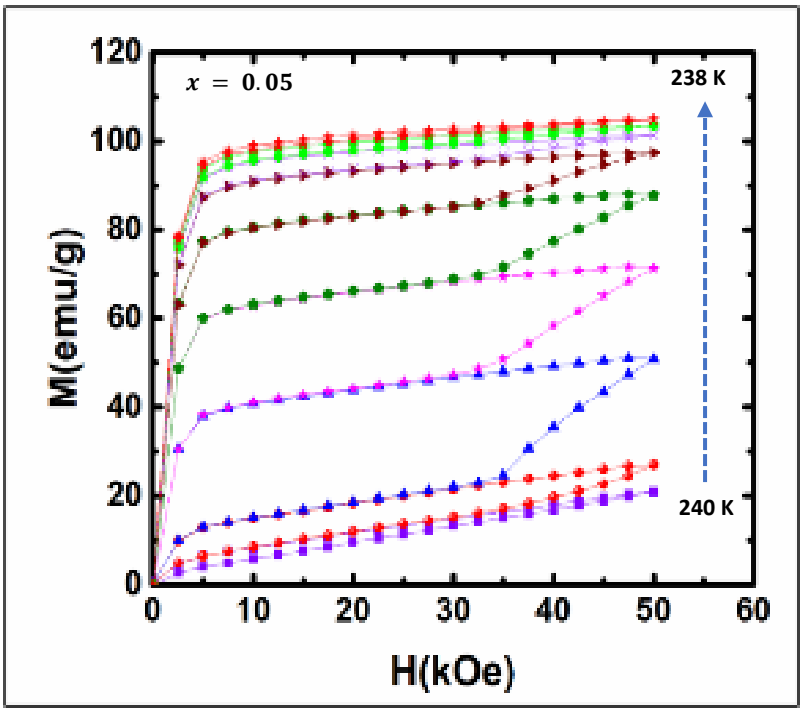

Fig. 4.18. Isothermal Magnetization versus field for annealed $Mn_{0.5}Fe_{0.5}Ni_{1-x}Co_xSi_{0.94}Al_{0.06}$ (x=0.05) obtained at various temperatures indicating magnetic hysteresis.

In order to ensure the nature of the phase transition, $M^2(T)$ data were collected at various temperatures for $Mn_{0.5}Fe_{0.5}Ni_{0.95}Co_{0.05}Si_{0.94}Al_{0.06}$ near the magnetic phase transition, and Arrott plot was plotted in Fig. 4.19(a) and Fig. 4.19 (b). During the cooling cycle in fig. 4.19(b), the S-shaped curve across the transition temperature demonstrated that the alloy undergoes a first order magnetic phase transition (FOMPT).[85] In the case of heating in fig. 4.19(a), the graph

exhibited a nonlinear dependence that was not S-shaped compared to cooling, indicating the first order behavior was weakened for the sample.

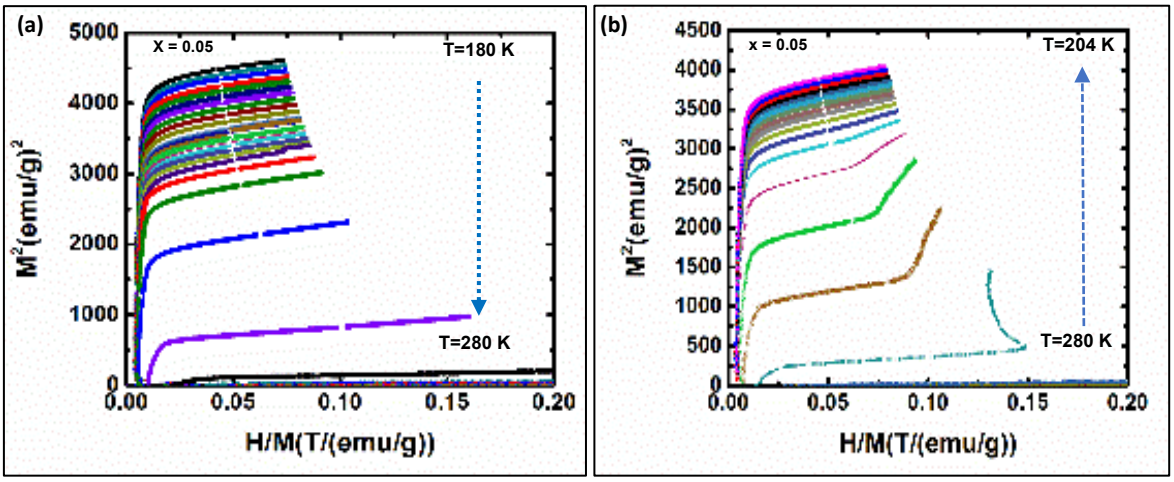

Fig. 4.19. M^2 versus H/M curve (Arrott Plot) for $Mn_{0.5}Fe_{0.5}Ni_{0.95}Co_{0.05}Si_{0.94}Al_{0.06}$ compound (a)heating and (b)cooling respectively.

M(H) data was obtained for powder $Mn_{0.5}Fe_{0.5}Ni_{1-x}Co_xSi_{0.94}Al_{0.06}$ (x=0.025) for as-cast and annealed sample for various temperature range under the magnetic field up to 50 kOe. For all samples field induced phase transition is observed during the cooling cycle, while at warming there is no magnetic hysteresis is observed. M(H) data for annealed powder $Mn_{0.5}Fe_{0.5}Ni_{1-x}Co_xSi_{0.94}Al_{0.06}$ (x=0.025) sample during heating and cooling is shown in Fig. 4.20(a) and Fig. 4.20(b). Saturation magnetization ~68 emu/g was measured from 230 K to 295 K temperature change during the warming while at cooling magnetization value was decreased at ~62 emu/g for 232 K to 300 K temperature change.

Magnetization slowly decreased with increasing temperature indicating the material is ferromagnetic. M(H) measurement was also performed for $Mn_{0.5}Fe_{0.5}Ni_{1-x}Cu_xSi_{0.94}Al_{0.06}$ (0.025, 0.075, 0.1) system. All samples exhibited similar ferromagnetic characteristics. x=0.025 and x=0.1 data is shown in Fig. 4.21(a) and Fig. 4.21(b). M(H) measurement was done using the same protocol. A magnetization value ~70 emu/g was obtained from 150 K to 235 K temperature (50 kOe) for x=0.025 which is decreased with concentration of x and magnetization was ~68 emu/g from 140 K to 260 K temperature range for x=0.1 sample (warming). Field induced hysteresis was measured from 190 K to 206 K temperature during for x=0.1 sample between magnetization and demagnetization process which is shown in Fig 4.22.

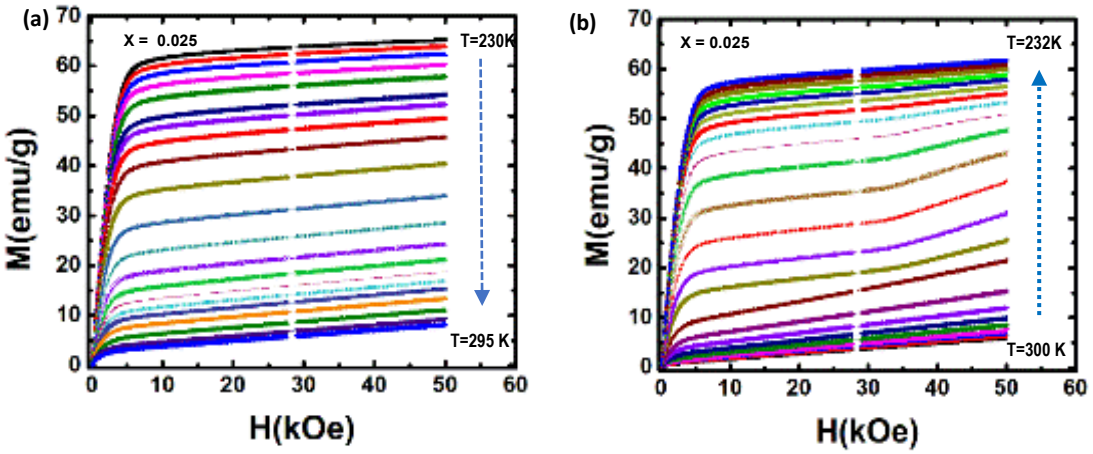

Fig. 4.20. Magnetization versus field for annealed powder $Mn_{0.5}Fe_{0.5}Ni_{1-x}Co_xSi_{0.94}Al_{0.06}$ (x=0.025) obtained at various temperatures near the first order phase transition at (a)warming and (b)cooling respectively.

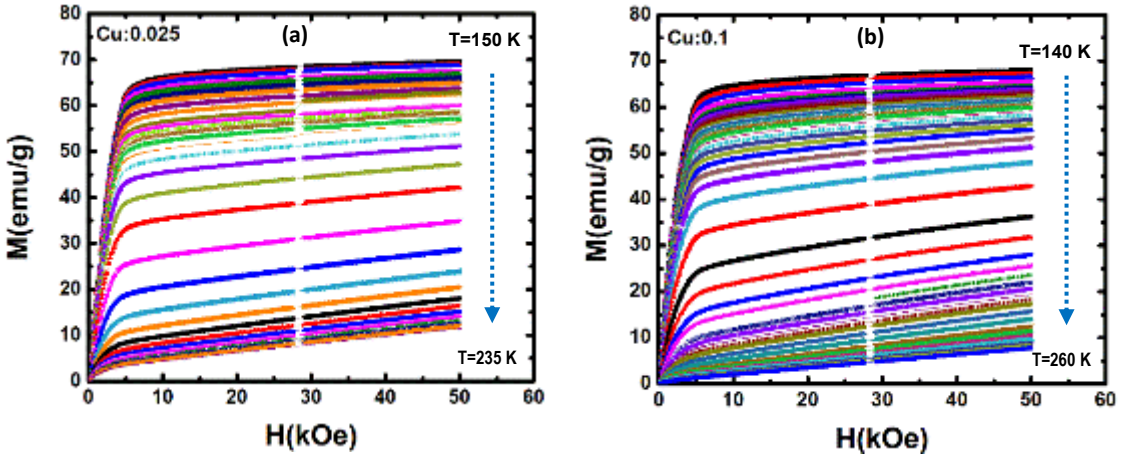

Fig. 4.21. Magnetization versus field for as-cast $Mn_{0.5}Fe_{0.5}Ni_{1-x}Cu_xSi_{0.94}Al_{0.06}$ for (a) x=0.025 and (b) x=0.1 compounds obtained at various temperatures near the first order phase

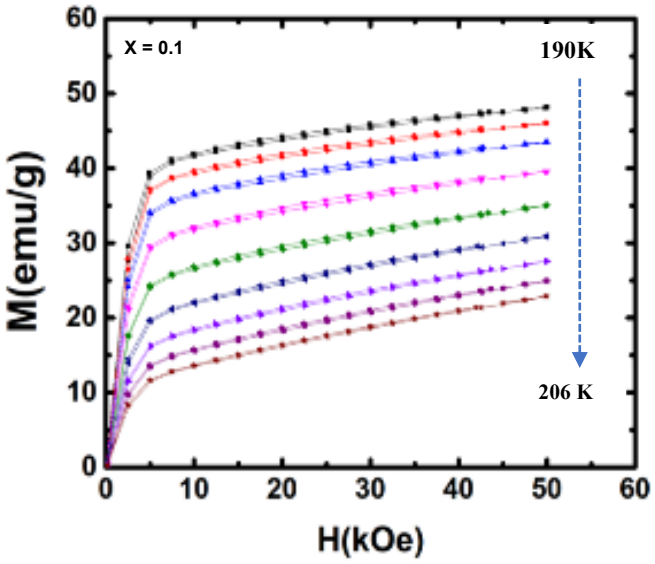

Fig. 4.22. Isothermal Magnetization versus field for $Mn_{0.5}Fe_{0.5}Ni_{1-x}Cu_xSi_{0.94}Al_{0.06}$ (x=0.1) obtained at various temperatures indicating magnetic hysteresis.

The temperature dependence of the magnetic entropy changes, ΔS_M (T), for various field change was determined by measuring the isothermal M(H) data as a function of increasing magnetic field. The Maxwell relation from equation 3.4 was used on the M(H) data to evaluate the ΔS_M(T) data for the $Mn_{0.5}Fe_{0.5}Ni_{1-x}Co_xSi_{0.94}Al_{0.06}$ (x=0.025, 0.05, 0.075) samples. The maximum ΔS_M value was obtained near phase transition temperature Tc due to the speedy change of magnetization around this temperature. Peak ΔS_M of -12.2 J kg^{-1} K^{-1} and -31.1 J kg^{-1} K^{-1} were observed for the as-cast x = 0.025 sample for field changes of ΔH = 20 kOe and 50 kOe, respectively [Fig. 4.23].

The annealed x = 0.025 sample showed peak values of -12.4 J kg^{-1} K^{-1} and -32.3 J kg^{-1} K^{-1} for ΔH = 20 kOe and 50 kOe, respectively for warming cycle. Although annealing did not have a significant effect on the ΔS_M for the sample with x = 0.025, it had a dramatic effect on the ΔS_M for the $Mn_{0.5}Fe_{0.5}Ni_{1-x}Co_xSi_{0.94}Al_{0.06}$ sample with x = 0.05. For ΔH = 20 kOe the peak value doubled from -8.2 J kg^{-1} K^{-1} (as cast) to -16.4 J kg^{-1} K^{-1} (annealed). The same was true for ΔH = 50 kOe, and the peak value changed from -21.6 J kg^{-1} K^{-1} (as cast) to -42.4 J kg^{-1} K^{-1} (annealed) for warming cycle which is shown in Fig. 4.24 respectively. ΔS_M reduced for annealed sample to -34 J kg^{-1} K^{-1} in $Mn_{0.5}Fe_{0.5}Ni_{1-x}Co_xSi_{0.94}Al_{0.06}$ (x=0.05) alloy during the cooling cycle for ΔH = 50 kOe. The peak ΔS_Ms for the $Mn_{0.5}Fe_{0.5}Ni_{1-x}Co_xSi_{0.94}Al_{0.06}$ samples at lower magnetic fields were also significantly large. For a field change of 10 kOe, the annealed x = 0.025 sample showed a peak ΔS_M of -5.7 J kg^{-1} K^{-1} [Fig. 4.23], and the annealed x = 0.05 sample showed a peak value of -7.4 J kg^{-1} K^{-1} [Fig.4.24]. Magnetic entropy value reduces with x for x=0.025 to x=0.05 as-cast sample and then increased for x=0.075. For annealed sample entropy linearly increased with x similar to the variation of Tc with x and it is shown in Fig. 4.25 for ΔH=50 kOe.

ΔS_M(T) data was obtained for powder as-cast and annealed $Mn_{0.5}Fe_{0.5}Ni_{1-x}Co_xSi_{0.94}Al_{0.06}$ (x=0.025) sample for heating and cooling cycle. Magnetic entropy is linearly increased with applied field. ΔS_M varied for powder as-cast and annealed sample in heating showing a peak of ΔS_M of 24.5 J kg^{-1} K^{-1} and -15.7 J kg^{-1} K^{-1} for ΔH=50 kOe respectively, which is shown in Fig. 4.26(a) and Fig. 4.26(b). Magnetic entropy decreases in the powder sample compared to the bulk sample. A peak ΔS_M of -9.5 J kg^{-1} K^{-1} was observed for warming which slightly reduced to -6 J kg^{-1} K^{-1} for 20 kOe magnetic field.

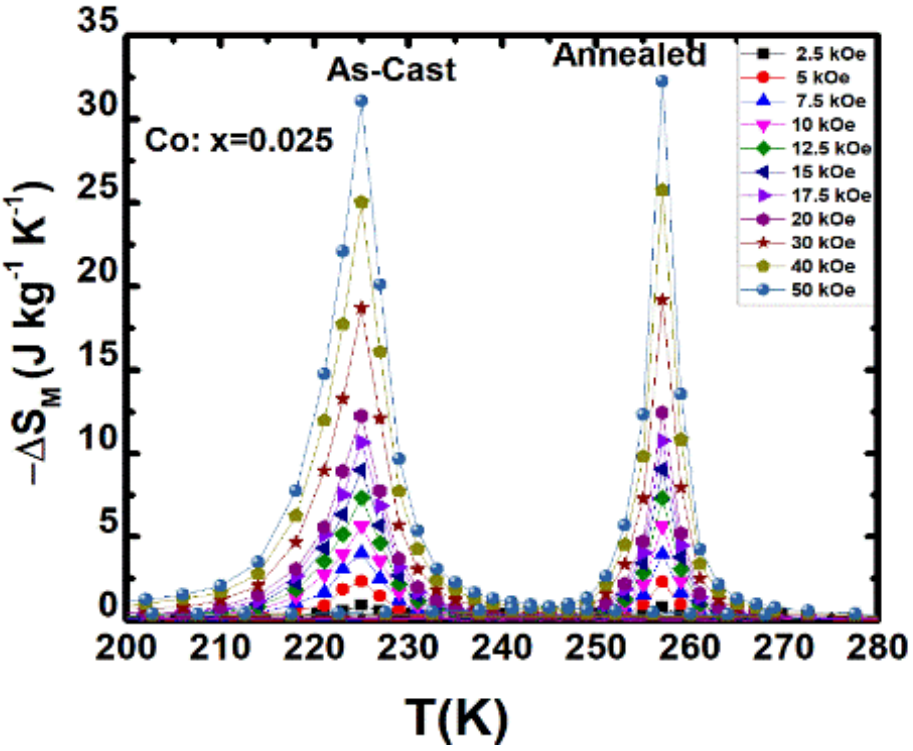

Fig. 4.23. The magnetic entropy changes as a function of temperature, $\Delta S_M(T)$, for $Mn_{0.5}Fe_{0.5}Ni_{1-x}Co_xSi_{0.94}Al_{0.06}$ (x=0.025).

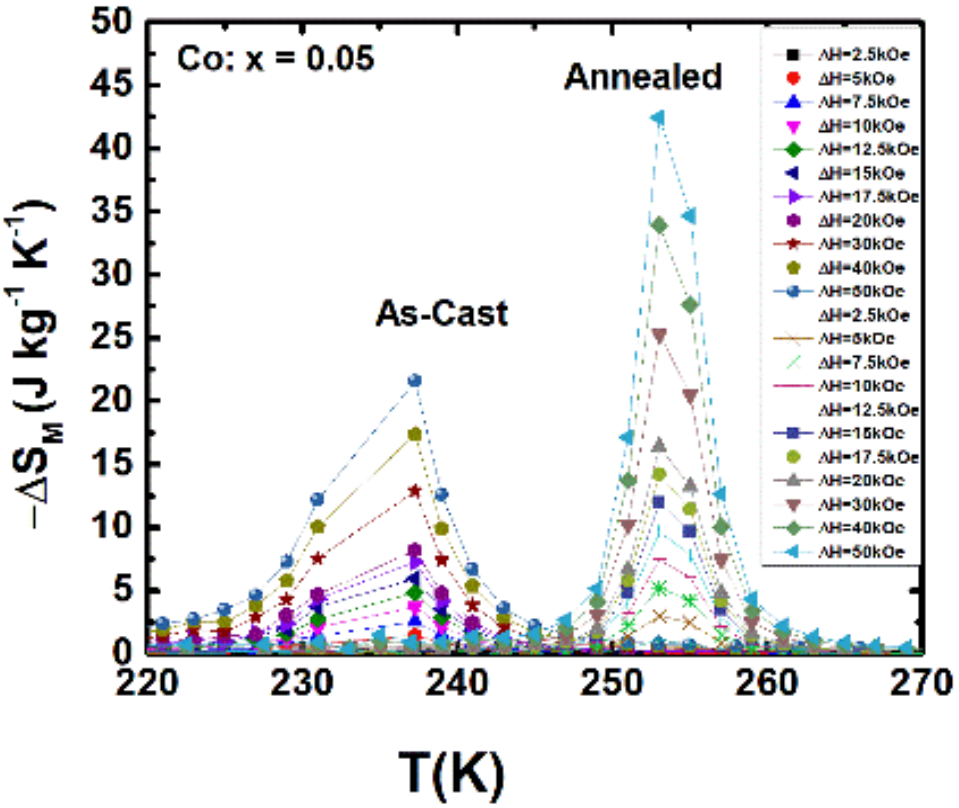

Fig. 4.24. The magnetic entropy changes as a function of temperature, ΔS_M (T), for $Mn_{0.5}Fe_{0.5}Ni_{1-x}Co_xSi_{0.94}Al_{0.06}$ (x=0.05).

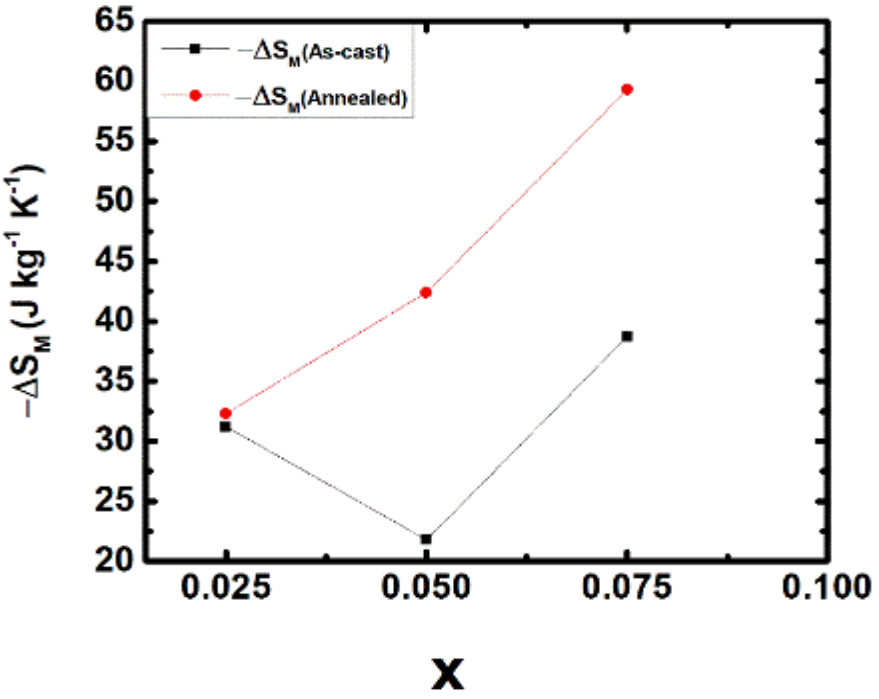

Fig. 4.25. Magnetic entropy changes with Co concentration x for $Mn_{0.5}Fe_{0.5}Ni_{1-x}Co_xSi_{0.94}Al_{0.06}$ (x= 0.025, 0.05, 0.075)

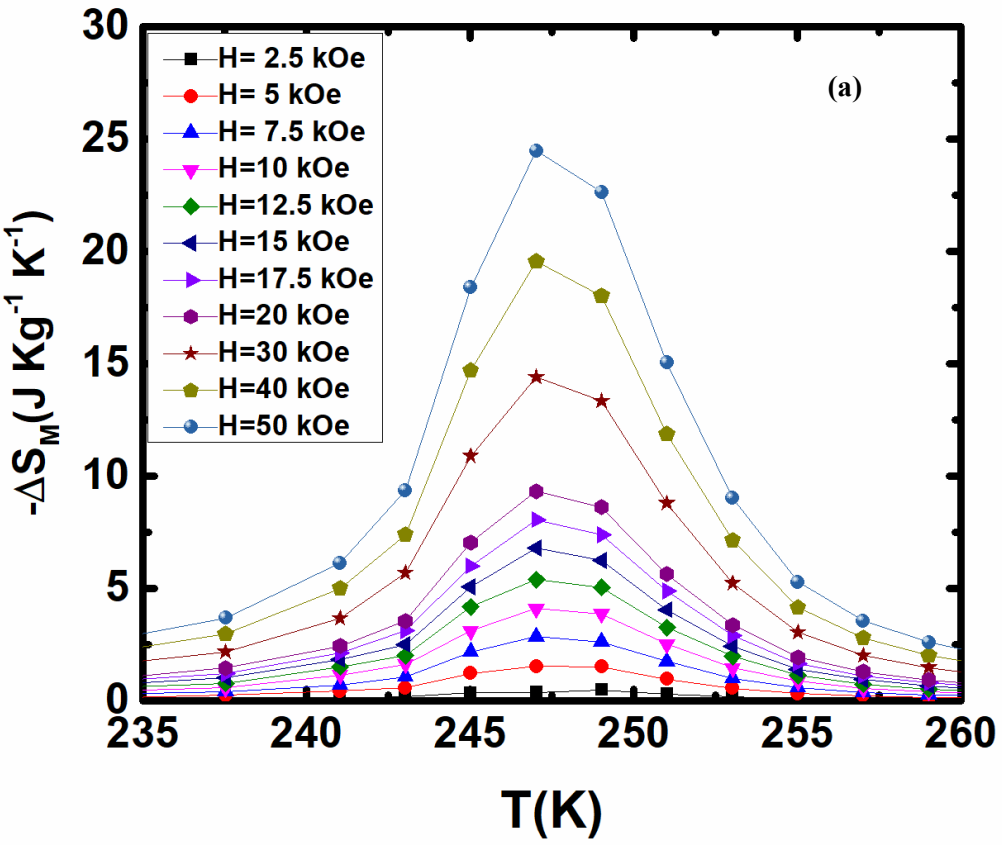

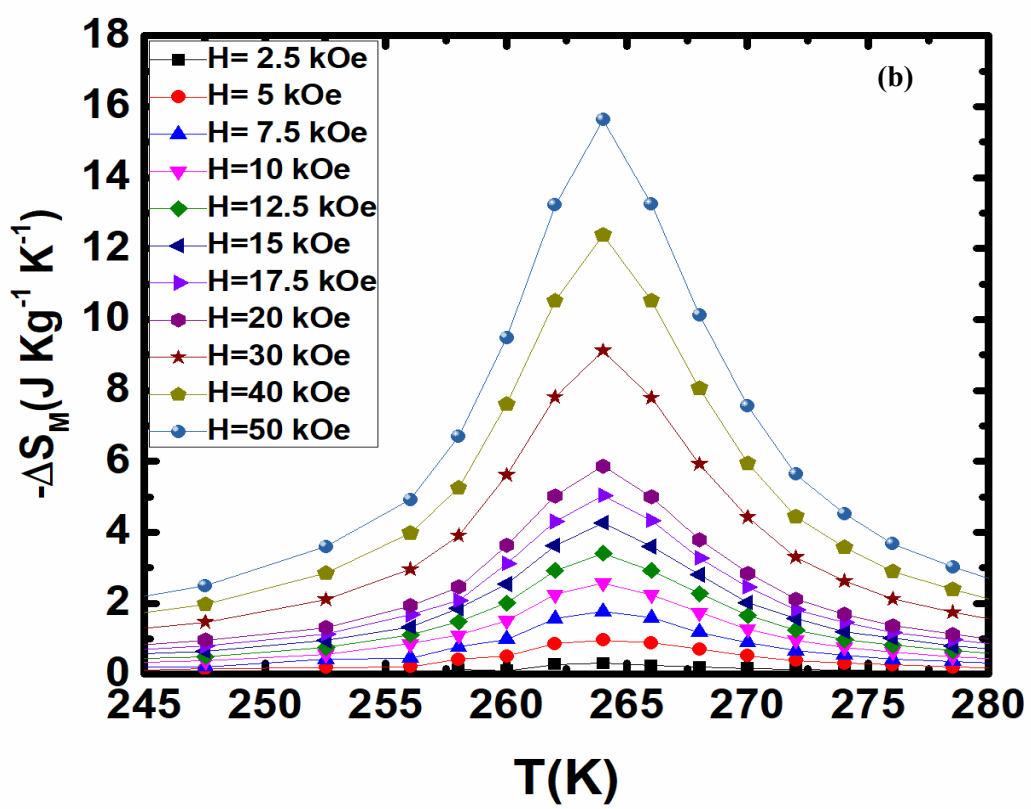

Fig. 4.26. The magnetic entropy changes as a function of temperature, $\Delta S_M(T)$, for powder (a) as-cast and (b) annealed $Mn_{0.5}Fe_{0.5}Ni_{1-x}Co_xSi_{0.94}Al_{0.06}$ (x=0.025) respectively.

Magnetic entropy changes as a function of temperature ΔS_M (T), for various field change was determined by measuring the isothermal M(H) data as a function of increasing magnetic field for the as-cast $Mn_{0.5}Fe_{0.5}Ni_{1-x}Cu_xSi_{0.94}Al_{0.06}$ (x=0.025, 0.75, 0.1) samples and shown in Fig. 4.27 and Fig. 4.28 for x=0.025 and x=0.01 respectively. A peak ΔS_M of -7 J kg^{-1} K^{-1} and -18.1 J kg^{-1} K^{-1} were observed for the as-cast x = 0.025 sample for field changes of ΔH = 20 kOe and 50 kOe respectively near phase transition where for x=0.1, Peak ΔS_M of -4.9 J kg^{-1} K^{-1} and -12.2 J kg^{-1} K^{-1} were observed for field changes of ΔH = 20 kOe and 50 kOe, respectively.

Temperature at which maximum entropy occurs is comparable to the value obtained at M(T). ΔS_M reduces with increment of x for (x=0.025 and x=0.075) and then increased for x=0.1 sample which is shown in Fig. 4.29. This behavior is not similar to the variation of Tc which decreases with x for this system.

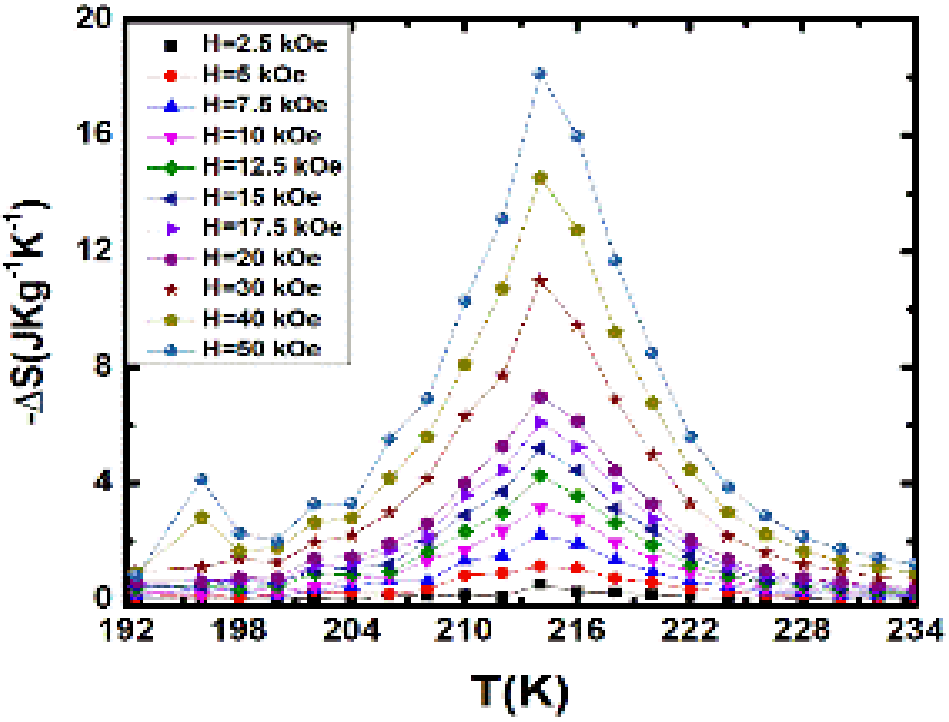

Fig. 4.27. The magnetic entropy changes as a function of temperature, ΔS_M (T), for as-cast $Mn_{0.5}Fe_{0.5}Ni_{1-x}Cu_xSi_{0.94}Al_{0.06}$ (x=0.025)

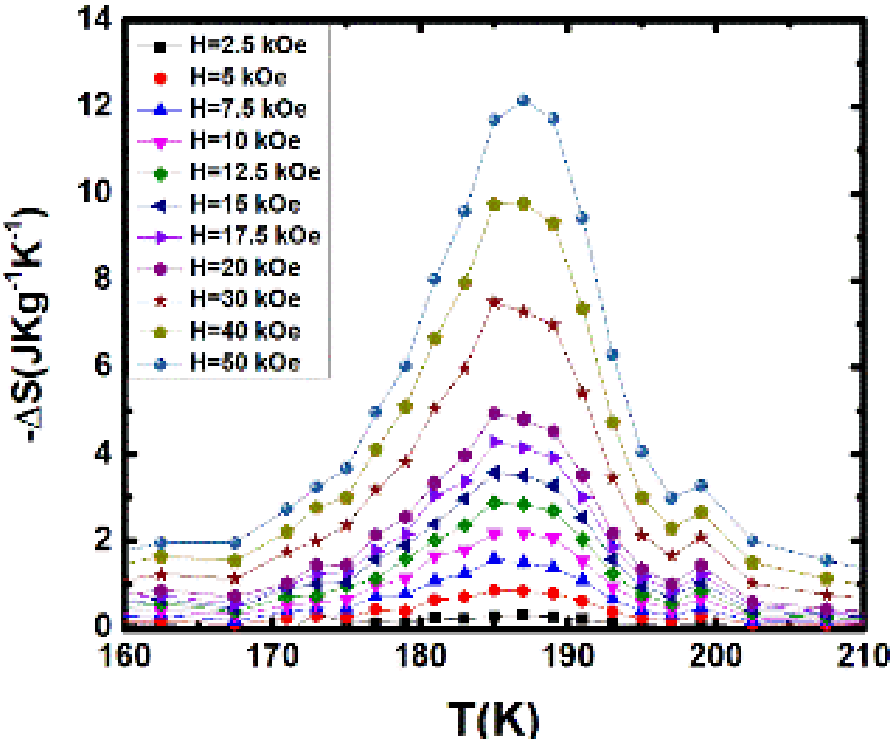

Fig. 4.28. The magnetic entropy changes as a function of temperature, ΔS_M(T), for as-cast $Mn_{0.5}Fe_{0.5}Ni_{1-x}Cu_xSi_{0.94}Al_{0.06}$ (x=0.1)

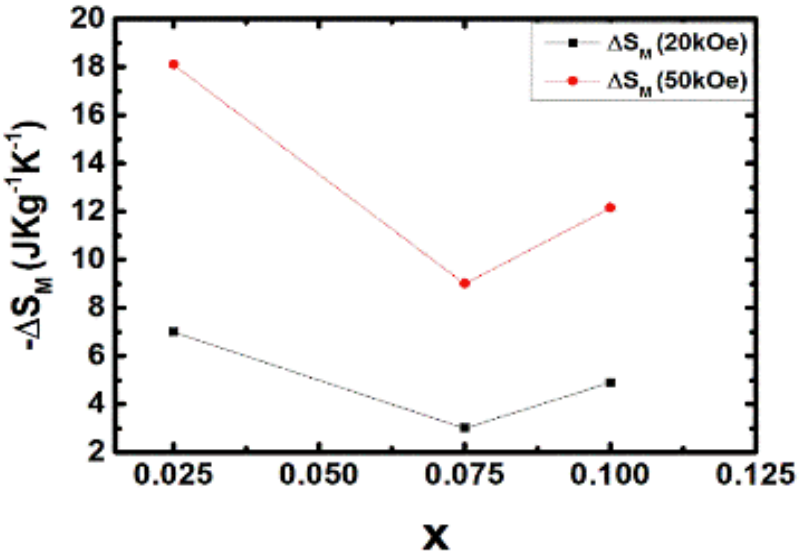

Fig. 4.29. Magnetic entropy changes with Cu concentration x for $Mn_{0.5}Fe_{0.5}Ni_{1-x}Cu_xSi_{0.94}Al_{0.06}$ (x= 0.025, 0.75, 0.1) at 20 kOe (black) and 50 kOe (red).

All these above mentioned values are either comparable or larger to numerous magnetocaloric compounds that exhibit similar or lower ΔS_M for much higher magnetic field changes.[86] Some The peak value ΔS_M of $Mn_{0.5}Fe_{0.5}Ni_{0.95}Co_{0.05}Si_{0.94}Al_{0.06}$ for 50 kOe and 20 kOe magnetic field are comparable to well-known magnetocaloric system such as $(La_{0.9}Sm_{0.1})_{0.67}Pb_{0.33}MnO_3$ compound exhibits a maximum ΔS_M of -4.31 J kg^{-1} K^{-1} near 340 K for a field change of 48 kOe,[87] while Gd_2In exhibits a ΔS_M of -4.5 J kg^{-1} K^{-1} near 188 K for a field change of 40 kOe.[88] More materials can be found for comparison in reference. [86]

Materials that exhibit phase transition near room temperature are desirable for MCE. A peak value ΔS_M of $Mn_{0.5}Fe_{0.5}Ni_{0.975}Cu_{0.025}Si_{0.94}Al_{0.06}$ for 50 kOe magnetic field have Tc around 216 K which is comparable to other reported system like $Mn_{1-x}Fe_xNiGe$ exhibits ΔS_M of -32 J kg^{-1} K^{-1} near 205 K temperature for a field change of 50 kOe.[89] $(MnNiSi)_{1-x}(FeCoGa)_x$ system exhibits ΔS_M of -23.8 J kg^{-1} K^{-1} near 213 K temperature for a field change of 50 kOe.[90] $Ni_{45.5}Co_2Mn_{37.5}Sn_{15}$ exhibits ΔS_M of -13.67 J kg^{-1} K^{-1} near 213 K temperature for a field change of 50 kOe.[91] All the samples reported in this thesis exhibit large MCE which is desirable for practical application in cooling technology.

Ideal magnetocaloric material $Gd_5(Si_2Ge_2)$ exhibits magnetic entropy change of -13 J kg^{-1} K^{-1} in comparatively low magnetic fields up to 2 T[3] and for higher magnetic field 5 T a peak of -18.4 J kg^{-1} K^{-1} is observed due to the first order phase transition near 276 k temperature. While

in pure gadolinium magnetic entropy changes of -10.2 J kg^{-1} K^{-1} is investigated for a field change of 5 T . Varying the Si and Ge concentration from 0.5 to 1.0, $Gd_5(Si_2Ge_2)$ compounds having a Curie temperature between 290 K and 335 K. These materials have the main disadvantages, their high price and significant hysteresis.

The refrigeration capacities (RC) for the $Mn_{0.5}Fe_{0.5}Ni_{1-x}Co_xSi_{0.94}Al_{0.06}$ and $Mn_{0.5}Fe_{0.5}Ni_{1-x}Cu_xSi_{0.94}Al_{0.06}$ samples were evaluated from the ΔS_M (T) data using the following expression,[92]

$$RC_{FWHM} = \int_{T_{Cold}}^{T_{Hot}} [\Delta S_M]_T \; dT$$

where T_{Hot} and T_{Cold} are defined as the temperature boundaries forming the full width at half maximum (FWHM) of the ΔS_M graph. This is the most used method for evaluating the RC from the ΔS_M curve. [93,94,95] For an applied magnetic field of 20 kOe, the annealed $Mn_{0.5}Fe_{0.5}Ni_{1-x}Co_xSi_{0.94}Al_{0.06}$ sample with x = 0.05 exhibited an RC of 64.2 J/kg, and for a field change of 50 kOe, the RC was 201 J/kg. The as-cast x = 0.05 sample and both the x = 0.025 samples exhibited lower RC values. Obtained value of RC with Co concentration is shown in Fig. 4.30 for a field change of 20 kOe and 50 kOe. For $Mn_{0.5}Fe_{0.5}Ni_{1-x}Cu_xSi_{0.94}Al_{0.06}$ sample exhibited RC of 188 J/kg and 174 J/kg for x=0.025 and x=0.01 for a field change of 50 kOe. The RCs for the $Mn_{0.5}Fe_{0.5}Ni_{1-x}Co_xSi_{0.94}Al_{0.06}$ and $Mn_{0.5}Fe_{0.5}Ni_{1-x}Cu_xSi_{0.94}Al_{0.06}$ compounds are comparable to those of numerous Heusler alloys including Ni_2MnIn, $Ni_{45}Co_5Mn_{36.6}In_{13.4}$, and even larger when compared to numerous others.[96,97]

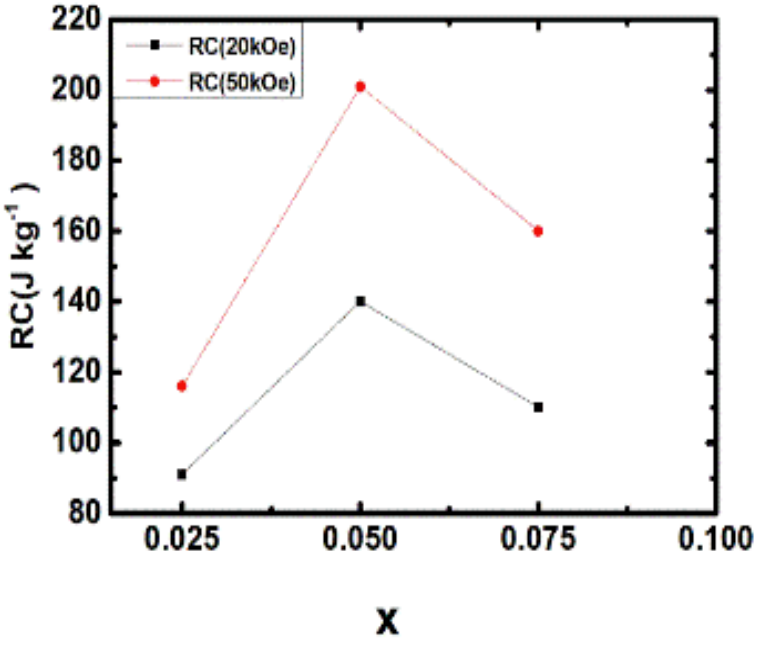

Fig. 4.30. Refrigeration capacity with Co concentration x for $Mn_{0.5}Fe_{0.5}Ni_{1-x}Co_xSi_{0.94}Al_{0.06}$ (x= 0.025, 0.05, 0.075).

Table 2: Magnetic Measurement Data of $Mn_{0.5}Fe_{0.5}Ni_{1-x}Co_xSi_{0.94}Al_{0.06}$, $Mn_{0.5}Fe_{0.5}Ni_{0.975}Co_{0.025}Si_{0.94}Al_{0.06}$ powder and $Mn_{0.5}Fe_{0.5}Ni_{1-x}Cu_xSi_{0.94}Al_{0.06}$ samples.

Co-doped As-cast Sample	Tc (K)		**Crystal Structure**	ΔS_M $(Jkg^{-1}K^{-1})$	
	Warming	**Cooling**		$\Delta H = 20kOe$	$\Delta H = 50kOe$
$Mn_{0.5}Fe_{0.5}Ni_{0.975}Co_{0.025}Si_{0.94}Al_{0.06}$	227 K	194 K	Hexagonal	- 12.2	- 31
$Mn_{0.5}Fe_{0.5}Ni_{0.95}Co_{0.05}Si_{0.94}Al_{0.06}$	236 K	206 K	Hexagonal	- 8.2	- 21.6
$Mn_{0.5}Fe_{0.5}Ni_{0.925}Co_{0.075}Si_{0.94}Al_{0.06}$	269 K	225 K	Hexagonal	- 15	- 38.7

Co-doped Annealed Sample	Tc (K)		**Crystal Structure**	ΔS_M $(Jkg^{-1}K^{-1})$	
	Warming	**Cooling**		$\Delta H = 20kOe$	$\Delta H = 50kOe$
$Mn_{0.5}Fe_{0.5}Ni_{0.975}Co_{0.025}Si_{0.94}Al_{0.06}$	258 K	232 K	Hexagonal	- 12.4	- 32.3
$Mn_{0.5}Fe_{0.5}Ni_{0.95}Co_{0.05}Si_{0.94}Al_{0.06}$	256 K	220 K	Hexagonal	- 16.4	- 42.4 warming - 34 cooling

Co Powder As-cast Sample	Tc (K)		**Crystal Structure**	ΔS_M $(Jkg^{-1}K^{-1})$	
	Warming	**Cooling**		$\Delta H = 20kOe$	$\Delta H = 50kOe$
$Mn_{0.5}Fe_{0.5}Ni_{0.975}Co_{0.025}Si_{0.94}Al_{0.06}$	254 K	230 K	Hexagonal	- 9.5 warming - 5.2 cooling	- 24.5 warming - 13.2 cooling

Co Powder Annealed Sample	Tc (K)		**Crystal Structure**	ΔS_M $(Jkg^{-1}K^{-1})$	
	Warming	**Cooling**		$\Delta H = 20kOe$	$\Delta H = 50kOe$
$Mn_{0.5}Fe_{0.5}Ni_{0.95}Co_{0.05}Si_{0.94}Al_{0.06}$	266 K	242 K	Hexagonal	- 6 warming - 6 cooling	- 15.7 warming - 15.5 cooling

Cu-doped As-cast Sample	Tc (K)		**Crystal Structure**	ΔS_M $(Jkg^{-1}K^{-1})$	
	Warming	**Cooling**		$\Delta H = 20kOe$	$\Delta H = 50kOe$
$Mn_{0.5}Fe_{0.5}Ni_{0.975}Cu_{0.025}Si_{0.94}Al_{0.06}$	216 K	192 K	Hexagonal	- 7	- 18.1
$Mn_{0.5}Fe_{0.5}Ni_{0.925}Cu_{0.075}Si_{0.94}Al_{0.06}$	208 K	190 K	Hexagonal	- 3	- 9
$Mn_{0.5}Fe_{0.5}Ni_{0.9}Cu_{0.1}Si_{0.94}Al_{0.06}$	196 K	174 K	Hexagonal	- 4.9	- 12.2

Chapter 5: Summary and Conclusion

In summary, we have investigated the structural and magnetic properties of the two series $Mn_{0.5}Fe_{0.5}Ni_{1-x}Co_xSi_{0.94}Al_{0.06}$ and $Mn_{0.5}Fe_{0.5}Ni_{1-x}Cu_xSi_{0.94}Al_{0.06}$ (x= 0, 0.025, 0.050, 0.075, 0.10) compound by partially substituting Ni with Co and Cu. Room temperature XRD data revealed that all the samples exhibited hexagonal crystal structure and lattice parameters varied marginally for all samples. SEM micrograph and EDS spectrum ensured that samples are highly homogenous with a satisfactory ratio of the targeted elements. For all samples, the first order nature of the phase transition is observed associated with thermal hysteresis. The phase transition temperature Tc increased for the as-cast sample and reduced for annealed sample in $Mn_{0.5}Fe_{0.5}Ni_{1-x}Co_xSi_{0.94}Al_{0.06}$ system with the substitution of Co. For $Mn_{0.5}Fe_{0.5}Ni_{1-x}Cu_xSi_{0.94}Al_{0.06}$ system, Tc increased with x which is similar to the powder $Mn_{0.5}Fe_{0.5}Ni_{0.975}Co_{0.025}Si_{0.94}Al_{0.06}$ sample. For $Mn_{0.5}Fe_{0.5}Ni_{1-x}Cu_xSi_{0.94}Al_{0.06}$ a peak ΔS_M of -18.1 J kg^{-1} K^{-1} was observed for x=0.1 sample for a field change of 50 kOe. A maximum magnetic entropy of -42.4 J kg^{-1} K^{-1} and RC value of 201 J/kg was observed in $Mn_{0.5}Fe_{0.5}Ni_{1-x}Co_xSi_{0.94}Al_{0.06}$ with x = 0.05 for a magnetic field change of 50 kOe near 256 K temperature during heating cycle where the entropy value was also higher in the cooling cycle with -34 $Jkg^{-1}K^{-1}$ for a field change of 50 kOe near 233 K temperature. $Mn_{0.5}Fe_{0.5}Ni_{0.975}Co_{0.025}Si_{0.94}Al_{0.06}$ powder system exhibited maximum entropy of 24.5 J kg^{-1} K^{-1} which is relatively lower than bulk sample. Based on the performed data coupled FOMPT was observed in all samples during heating and cooling with high MCE which is desirable for magnetic refrigeration technology.

Reference

[1] V. Franco, J.S. Blázquez, B. Ingale, and A. Conde, Annu. Rev. Mater. Res. **42**, 305 (2012).

[2] V. Franco, J.S. Blázquez, J.J. Ipus, J.Y. Law, L.M. Moreno-Ramírez, and A. Conde, Prog. Mater. Sci. **93**, 112 (2018).

[3] V.K. Pecharsky and K.A. Gschneidner Jr, Phys. Rev. Lett. **78**, 4494 (1997).

[4] Z.D. Han, D.H. Wang, C.L. Zhang, S.L. Tang, B.X. Gu, and Y.W. Du, Appl. Phys. Lett. **89**, 182507 (2006).

[5] B.G. Shen, J.R. Sun, F.X. Hu, H.W. Zhang, and Z.H. Cheng, Adv. Mater. **21**, 4545 (2009).

[6] E. Brück, M. Ilyn, A.M. Tishin, and O. Tegus, J. Magn. Magn. Mater. **290–291**, 8 (2005).

[7] F. Hu, B. Shen, J. Sun, and G. Wu, Phys. Rev. B **64**, 132412 (2001).

[8] N.A. Zarkevich and V.I. Zverev, Crystals **10**, 815 (2020).

[9] N. A. Zarkevich, D. D. Johnson, V. K. Pecharsky, J. Phys. D Appl. Phys. **51,** 024002 (2017).

[10] F. Scheibel, T. Gottschall, A. Taubel, M. Fries, K. P. Skokov, A. Terwey, W. Keune, K. Ollefs, H. Wende, M. Farle, M. Acet, O. Gutfleisch, M. E. Gruner, Energy Technol 6, 1397 (2018).

[11] Á. Díaz-García, L.M. Moreno-Ramírez, J.Y. Law, F. Albertini, S. Fabbrici, V. Franco. Journal of Alloys and Compounds, Volume 867, 159184, (2021).

[12] Das, Ranjit Chandra, MS Thesis http://orcid.org/0000-0002-2041-4759 (2021).

[13] Babajide Olaolu Akintunde, MS Thesis http://orcid.org/0000-0003-1379-5319 (2021).

[14] Bishnu R. Dahal, Zachary Lehmann, Yung Huh, and Parashu Kharel AIP Advances 10, 015109 (2020).

[15] O. Gutfleisch, T. Gottschall, M. Fries, D. Benke, I. Radulov, K. P. Skokov, H. Wende, M. Gruner, M. Acet, P. Entel, and M. Farle Phil. Trans. R. Soc. A. 374: 20150308. (2016).

[16] http://www.tikalon.com/blog/blog.php?article=2014/magnetic_cooling.

[17] S. K. Panda, Su. Datta, S. Guha, J. Mallick, and M. Kar, Phys. Rev. Applied **16**, 064027 (2021).

[18] S. Ghosh, S. Samanta, J. S. Mohanty, J. Sinha, and K. Mandal, J. Appl. Phys. 132, 045001 (2022).

[19] A. Biswas, A.K. Pathak, N.A. Zarkevich, X. Liu, Y. Mudryk, V. Balema, D.D. Johnson, and V.K. Pecharsky, Acta Mater. **180**, 341 (2019).

[20] J. Liu, Y. Gong, G. Xu, G. Peng, I.A. Shah, N. Ul Hassan, and F. Xu, Sci. Rep. **6**, 1 (2016).

[21] M.L. Arreguín-Hernández, C.F. Sánchez-Valdés, and J.L. Sánchez Llamazares, J. Magn. Magn. Mater. **533**, 168021 (2021).

[22] N.T. Trung, L. Zhang, L. Caron, K.H.J. Buschow, and E. Brück, Appl. Phys. Lett. **96**, 172504 (2010).

[23] T. Samanta, I. Dubenko, A. Quetz, S. Stadler, and N. Ali, Appl. Phys. Lett. **101**, 242405 (2012).

[24] Z. Y. Wei, E. K. Liu, Y. Li, G. Z. Xu, X.-M. Zhang, G. D. Liu, X.-K. Xi, H. W. Zhang, W.H. Wang, G. H. Wu, and X. Zhang, Adv. Electron. Mater. **1**, 1500076 (2015).

[25] A.P. Sivachenko, V.I. Mityuk, V.I. Kamenev, A.V. Golovchan, V.I. Val'kov, and I.F. Gribanov, Low Temp. Phys. **39**, 1051 (2013).

[26] B. D. Cullity and C. D. Graham, "Introduction to Magnetic Materials," (2nd Edition, Wiley, Hoboken, 2009).

[27] R. C. O'Handley, Modern Magnetic Materials. Hoboken, NJ: Wiley (2000).

[28] D. L. Sidebottom, "Fundamentals of Condensed Matter and Crystalline Physics," (Cambridge Univ. Press, New York, 2012).

[29] Magnetic, Ferroelectric, and Multiferroic Metal Oxides. A volume in Metal Oxides https://doi.org/10.1016/C2016-0-00851-3.

[30] M. Kumari, magnetic properties of iron-oxide nanoparticles and methods for their characterization, ETH ZURICH, (2015).

[31] Allan H. Morrish The Physical Principles of Magnetism; ISBN: 978-0-780-36029-7 (2001) https://books.google.com/books/about/The_Physical_Principles_of_Magnetism.html?id=ZjUbAQAAIAAJ.

[32] C. Kittle, Introduction to Solid State Physics.

[33] https://link.springer.com/book/10.1007/978-3-031-32084-2.

[34] K. H. J. Buschow and F. R. De Boer, "Magnetism and Magnetic Materials," (Kluwer Academic Publishers, New York, 2004).

[35] N. A. Spaldin, "Magnetic Materials: Fundamentals and Applications," (2nd Edition, Cambridge Univ. Press, New York, 2010).

[36] C. Stefanita, Magnetism: Basics and Applications, (Springer, Berlin, 2012).

[37] Agbo, Sunday A, Phase Transitions and Associated Magnetic and Transport Properties in Selected Ni-Mn-Ga based Heusler Alloy; http://orcid.org/0000-0001-8832-4533 (2020).

[38] Brock, J. A., An experimental study of magnetic and structural phase transitions and associated phenomena in selected Ni-Mn-derivative Heusler alloys; http://orcid.org/0000-0003-1871-8961. (2017).

[39] M.A. Ruderman and C. Kittel, Phys. Rev. 96, 99 (1954).

[40] J. M. D. Coey, "Magnetism and Magnetic Materials," (Cambridge Univ. Press, New York, 2009).

[41] Superexchange Interation and Symmetry Properties of Electron Orbitals Junjiro Kanamori https://doi.org/10.1016/0022-3697(59)90061-7.

[42] H. Kramers Superexchange interaction and symmetry properties of electron orbitals, Vol 10, https://doi.org/10.1016/0022-3697(59)90061-7 (1934).

[43] P.W. Anderson, Antiferromagnetism. Theory of Superexchange Interaction; Phys. Rev. 79, 350 (1950).

[44] C. Zner Interaction between the d-Shells in the Transition Metals. II. Ferromagnetic Compounds of Manganese with Perovskite Structure Rev. 82, 403 (1951).

[45] E. Warburg, Magnetische, Ann. Phys. 13, 141 (1881).

[46] P. Weiss and A. Piccard, J. Phys. Theor. Appl. 7, 103 (1917).

[47] W.F. Giauque, A Thermodynamic treatment of certain magnetic effects. A proposed method of producing temperatures considerably below 1° absolute, J. Am. Chem. Soc. 49 (1927) 1864–1870. https://pubs.acs.org/doi/10.1021/ja01407a003.

[48] W.F. Giauque, D.P. MacDougall, Attainment of temperatures below 1° absolute by demagnetization of $Gd_2(SO_4)_3.8H_2O$, Phys. Rev. 43 (1933) 768. https://doi.org/10.1103/PhysRev.43.768.

[49] Pecharsky, V.K. and Gschneidner Jr, K.A., 1997. Giant magnetocaloric effect in Gd5(Si2Ge2). Physical review letters, 78(23), p.4494.

[50] The Magnetocaloric Effect and its Applications, by A.M. Tishin, Y.I. Spichkin (2003) https://doi.org/10.1201/9781420033373.

[51] A. Kitanovski, J. Tušek, U. Tomc, U. Plaznik, M. Ozbolt, and A. Poredoš, "Magnetocaloric Energy Conversion: From Theory to Applications," (Springer, Switzerland, 2015). https://doi.org/10.1007/978-3-319-08741-2.

[52] Blundell, Stephen J.; Katherine M. Blundel. Concepts in Thermal Physics. Oxford University Press, Oxford (2008).

[53] Law, J.Y., Franco, V., Moreno-Ramírez, L.M. et al. Nat Commun 9, 2680 (2018). https://doi.org/10.1038/s41467-018-05111-w.

[54] V. J. Vodyanoy, Y. Mnyukh the Physical Nature of "Giant" Magnetocaloric and Electrocaloric Effects (2013).

[55] Y. Mnyukh Hysteresis and nucleation in condensed matter (2011).

[56] Y. Mnyukh, Fundamentals of Solid-State Phase Transitions, Ferromagnetism and Ferroelectricity (2001) [or 2nd (2010) Edition].

[57] N. A. de Oliveira, P. J. von Ranke, Theoretical aspects of the magnetocaloric effect, Phys. Reports, 489, 89-159 (2010).

[58] Y. Mnyukh, Ferromagnetic State and Phase Transitions, doi: 10.5923/j.ajcmp.20120205.01 (2012).

[59] Morellon, L.; Arnold, Z.; Magen, C.; Ritter, C.; Prokhnenko, O.; Skorokhod, Y.; Algarabel, P.A.; Ibarra, M.R.; Kamarad, J. Pressure enhancement of the giant magnetocaloric effect in $Tb_5Si_2Ge_2$. *Phys. Rev. Lett.* **2004**, *93*, 137201 (2004).

[60] Pasquale, M.; Sasso, C.P.; Lewis, L.H.; Giudici, L.; Lograsso, T.; Schlagel, D. Magnetostructural transition and magnetocaloric effect in $Ni_{55}Mn_{20}Ga_{25}$ single crystals. *Phys. Rev. B* **2005**, *72*, 094435.

[61] Zhou, X.Z.; Li, W.; Kunkel, H.P.; Williams, G. A criterion for enhancing the giant magnetocaloric effect: (Ni-Mn-Ga)—A promising new system for magnetic refrigeration. *J. Phys.-Condens. Matter* **2004**, *16*, L39–L44 (2004).

[62] Fujita A, Fujieda S, Hasegawa Y, Fukamichi K. Itinerant-electron metamagnetic transition and large magnetocaloric effects in $La(Fe_xSi_{1-x})_{13}$ compounds and their hydrides. *Phys. Rev. B.* 67(10): https://doi.org/10.1103/physrevb.67.104416.

[63] Huu, C.X. Chau, N. The, N.D. Hoa, N.Q. Giant magnetocaloric effect at room temperature and low-field change in $Fe_{78-x}Cr_xSi_4Nb_5B_{12}Cu_1$ amorphous alloys. *J. Korean Phys. Soc.* **2008**, *53*, 763–765.

[64] Chau, N.; Thanh, P.Q.; Hoa, N.Q.; The, N.D. The existence of giant magnetocaloric effect and laminar structure in $Fe_{73.5-x}Cr_xSi_{13.5}B_9Nb_3Cu_1$. *J. Magn. Magn. Mater.* **2006**, *304*, 36–40.

[65] Liu, J.; Gong, Y.Y.; You, Y.R.; You, X.M.; Huang, B.W.; Miao, X.F.; Xu, G.Z.; Xu, F.; Bruck, E. Giant reversible magnetocaloric effect in MnNiGe-based materials: Minimizing thermal hysteresis via crystallographic compatibility modulation. *Acta Mater.* **2019**, *174*, 450–458.

[66] Li, Z.B.; Zhang, Y.D.; Sanchez-Valdes, C.F.; Llamazares, J.L.S.; Esling, C.; Zhao, X.; Zuo,L. Giant magnetocaloric effect in melt-spun Ni-Mn-Ga ribbons with magneto-multistructural transformation. *Appl. Phys. Lett.* **2014**, *104*, 044101.

[67] J. Rodríguez-Carvajal, Physica B: Condens. Matter **192**, 55 (1993).

[68] X-ray reflection in accordance with Bragg's Law D. Henry, N. Eby, J. Goodge, D. Mogk https://serc.carleton.edu/msu_nanotech/methods/BraggsLaw.html.

[69] X-ray Powder Diffraction (XRD) B. L. Dutrow, C. M. Clark, https://serc.carleton.edu/research_education/geochemsheets/techniques/XRD.html#:~:text=X%2Dray%20diffraction%20is%20based,and%20directed%20toward%20the%20sample.

[70] Crystallography Open Database http://www.crystallography.net/cod.

[71] Scanning Electron Microscopy and X-Ray Microanalysis. Joseph I. Goldstein, Dale E. Newbury, Patrick Echlin, David C. Joy, A. D. Romig, Charles E. Lyman, Charles Fiori, Eric Lifshin.

[72] Pandit, P.P.; Liu, C.; Iacono, S.; Corti, G.; Hu, Y. Microstructural Characterization and Property of Carbon Fiber Reinforced High-Density Polyethylene Composites Fabricated by Fused Deposition Modeling. Materials 2023, 16, 180. https://doi.org/10.3390/ma16010180.

[73] On Moseley's Law for X-Ray Spectra by Horace Scudder Uhler Pnas Vol 3(2) 88-90 February 1, 1917 https://doi.org/10.1073/pnas.3.2.88.

[74] V.K. Pecharsky and K.A. Gschneidner Jr, J. Appl. Phys. **90**, 4614 (2001).

[75] Physical Property Measurement System, Hardware Manual, Quantum Design Inc. P.H. 1070-150, Rev. B5 (2008).

[76] An experimental study on the magnetic and exchange bias properties of selected Mn rich Ni-Mn-Ga based Heusler Alloys. by A. M. Albagami, MS thesis, Miami University (2016).

[77] Vibrating sample magnetometry Practical for the European School on Magnetism (2019) https://magnetism.eu/esm/2019/practical/VSM_practical.pdf.

[78] Vibrating Sample Magnetometery: Analysis and Construction by S. A. H. Shah, LUMS (2013) https://physlab.org/wp-content/uploads/2016/03/Sproj_alamdar1.pdf.

[79] Mahmud Khan, Ranjit Chandra Das, Jacob Casey, Brandon L. Reese, Babajide Akintunde, Arjun K. Pathak; Near room temperature magnetocaloric properties in Ni deficient (Mn0.525Fe0.5)Ni0.975Si0.95Al0.05. AIP Advances 1 March 2022; 12 (3): 035227. https://doi.org/10.1063/9.0000294.

[80] Richard J. D. Tilley Crystals and Crystal Structures, Wiley 2nd edition ISBN 9781119548591 (2020).

[81] S. Bhattacharjee N. Kramer, C. Hanley, Arjun K. Pathak, Mahmud Khan, AIP Advances 13, 025236 (2023).

[82] Liu, J., Gong, Y., Xu, G., Peng, G., Shah, I.A., Ul Hassan, N. and Xu, F., 2016. Realization of magnetostructural coupling by modifying structural transitions in MnNiSi CoNiGe system with a wide Curie-temperature window. Scientific reports, 6(1), pp.1-8.

[83] A. Biswas, A.K. Pathak, N.A. Zarkevich, X. Liu, Y. Mudryk, V. Balema, D.D. Johnson, and V.K. Pecharsky, Acta Mater. **180**, 341 (2019).

[84] V. Chaudhary, X. Chen, R.V. Ramanujan, Prog. Mater. Sci. **100**, 64 - 98 (2019).

[85] N. H. Duc, D. T. Kim Anh and P. E. Brommer, Physica B. 319 (2002).

[86] N.R. Ram, M. Prakash, U. Naresh, N.S. Kumar, T.S. Sarmash, T. Subbarao, R.J. Kumar, G.R. Kumar, and K.C.B. Naidu, J. Supercond. Nov. Magn. **31**, 1971 (2018).

[87] S. K. Çetin, M. Acet, M. Günes, A. Ekicibil, M. Farle, J. Alloys Compd. **650**, 285 (2015).

[88] S. Tencé, B. Chevalier, J. Magn. Magn. Mater. **399**, 46–50 (2016).

[89] E. Liu, W. Wang, L. Feng, W. Zhu, G. Li, J. Chen, H. Zhang, G. Wu, C. Jiang, H. Xu, and F. de Boer, Stable magnetostructural coupling with tunable magnetoresponsive effects in hexagonal ferromagnets, Nat. Commun. 3, 873 (2012).

[90] S. Ghosh, A. Ghosh, P. Sen, and K. Mandal, Giant RoomTemperature Magnetocaloric Effect Across the MagnetoStructural Transition in (MnNiSi)1−x(FeCoGa)x Alloys, Phys. Rev. Appl. 14, 014016 (2020).

[91] S. Arumugam, S. Ghosh, A. Ghosh, U. Devarajan, M. Kannan, L. Govindaraj, and K. Mandal, Effect of hydrostatic pressure on the magnetic, exchange bias and magnetocaloric properties of Ni45.5Co2Mn37.5Sn15, J. Alloys Compd. 712, 714 (2017).

[92] K.A. Gschneidner Jr and V.K. Pecharsky, Annu. Rev. Mater. Sci. **30**, 387 (2000).

[93] A.L. Lima Sharma, P.A. Sharma, S.K. McCall, S.-B. Kim, and S.-W. Cheong, Appl. Phys. Lett. **95**, 092506 (2009).

[94] X.C. Zhong, P.F. Tang, Z.W. Liu, D.C. Zeng, Z.G. Zheng, H.Y. Yu, W.Q. Qiu, H. Zhang, and R.V. Ramanujan, J. Appl. Phys. **111**, 07A919 (2012).

[95] H. Zhang, R. Li, T. Xu, F. Liu, and T. Zhang, J. Magn. Magn. Mater. **347**, 131 (2013).

[96] J. Brock and M. Khan, J. Magn. Magn. Mater. **425**, 1 (2017).

[97] T. Ryba, Z. Vargova, R. Varga, V. Zhukova, and A. Zhukov, IEEE Trans. Magn. **49**, 54 (2013).